 doi:10.20944/preprints201903.0034.v1

Type of the Paper (Article)

Thermophysical characterization and numerical investigation of three paraffin waxes as Latent Heat Storage Materials.

Manel Kraiem[1,2], Mustapha Karkri[1*], Sassi Ben Nasrallah[2], Patrik SOBOLCIAK[3], Magali FOIS[1], Nasser A. Alnuaimi[3]

[1] Université Paris-Est, Centre d'Etudes et de Recherche en Thermique, Environnement et Systèmes (CERTES), EA3481, 61 Avenue du Général de Gaulle, 94010 Créteil Cedex, France.
[2] Université de Monastir, Ecole Nationale d'Ingénieurs de Monastir, Laboratoire d'Etudes des Systèmes Thermiques et Energétiques (LESTE), LR99ES31, Avenue Ibn El Jazzar, 5019 Monastir, Tunisie.
[3] Qatar University, Center of Advanced Materials, 2713 Doha, Qatar.
* Correspondence: Corresponding author: mustapha.karkri@u-pec.fr;

Abstract: Thermophysical characterization of three paraffin waxes (RT27, RT21 and RT35HC) is carried out in this study using DSC, TGA and transient plane source technics. Then, a numerical study of their melting in a rectangular enclosure is examined. The enthalpy-porosity approach is used to formulate this problem in order to understand the heat transfer mechanism during the melting process. The analysis of the solid-liquid interface shape, the temperature field shows that the conduction is the dominant heat transfer mode in the beginning of the melting process. It is followed by a transition regime and the natural convection becomes the dominant heat transfer mode. The effects of the Rayleigh number and the aspect ratio of the enclosure on the melting phenomenon are studied and it is found that the intensity of the natural convection increases as the Rayleigh number is higher and the aspect ratio is smaller. In the second part of the numerical study, a comparison of the performance of paraffins waxes during the melting process is conducted. Results reveals that from a kinetically RT21 is the most performant but in term of heat storage capacity, it was inferred that RT35HC is the most efficient PCM.

Keywords: Phase change material, Paraffin, Melting, Natural convection, Thermal storage.

1. Introduction

Latent heat thermal energy storage systems (LHTESS) using solid-liquid phase change materials PCMs attract a great growing interest in many applications [1,2] such as passive systems for buildings, active systems for buildings, solar thermal systems and thermal control of electronic devices. The attention accorded to these materials is prompted by their capabilities to store and to release a large amount of energy at a nearly constant temperature during the melting and the solidification process. The performance of systems using PCMs is controlled by the thermal behavior of these materials within the solid-liquid phase change phenomenon. That's why a thorough understanding and analysis of the heat transfer characteristics during the melting and the solidification of PCM is strongly required. In this context, several studies were dedicated to understand the heat transfer's modes during the solid-liquid phase change process and to analyze the key parameters controlling this phenomenon. In fact, many researches have been conducted to study the melting process of PCMs in a rectangular enclosure. They are classified into two groups according to the imposed boundary conditions: ***constant temperature***, ***constant flux***. Regarding to the first group, Jellouli et al. [3] performed a numerical study of the melting process of a PCM with in a rectangular cavity heated from the bottom at a constant temperature. The natural convection was taken into account in the liquid PCM. Results showed that at an early stage of the melting process, the heat transfer is dominated by conduction. Then, the natural convection became the dominant heat transfer mode and its effect was intensified as the thickness of the melted layer increased.

 doi:10.20944/preprints201903.0034.v1

Shokouhmand and Kamkari [4] investigated an experimental study of the melting of lauric acid in a rectangular enclosure heated isothermally at its vertical wall. The visualization of the solid-liquid interface by a digital camera and the measurement of the temperatures during this process showed that the melting phenomenon is characterized by four successive stages (conduction, transition, strong natural convection, weak convection). Ho et al. [5] studied numerically and experimentally the melting of n-octadecane in a vertical rectangular enclosure with a free moving ceiling. The main findings of this study were that the strength of the natural convection increases as the Rayleigh number increases and as the aspect ratio decreases.

Concerning the second type of boundary conditions, Zhang et al. [6] studied experimentally the melting of n-octadecane in a rectangular cavity with one wall subjected to a constant heat flux. The main findings of this study were that the morphology of the solid-liquid interface is strongly affected by the natural convection during the melting process and the intensity of the natural convection increases as the Rayleigh number increases. Jianhua et al. [7] reported an experimental study of the melting of n-octadecane in a rectangular enclosure heated from the bottom with three heat sources. It was found that the melting process is more rapid as the aspect ratio decreases. Sun et al. [8] investigated experimentally the melting of n-octadecane in a square cavity heated by light bulbs in order to determine the increase of the heat transfer induced by the natural convection in the liquid PCM. It was showed that the heat transfer coefficient when the natural convection is taking into account is higher than when the only considered heat transfer mode is the conduction.

Regarding to the investigations which studied the melting process of PCMs in a spherical enclosure, Aadmi et al. [9] reported a combined numerical and experimental study of the melting process of paraffin wax RT27 in a spherical geometry. It was revealed that the melting process depends on the diameter of the sphere. Archibold et al. [10] conducted a numerical study of the melting process of sodium nitrate in a spherical enclosure. A parametric analysis of the effect of the Rayleigh number on the thermal behavior of capsules with different diameters was performed. It was claimed that the melt fraction rate of NaNO3 increases as the Rayleigh number increases. From the above literature review, although many numerical and experimental investigations were devoted to the study of the thermal behavior of different PCMs during the melting process in various geometries, there is no study of the heat transfer characteristics of RT27, RT21 and RT35HC within the melting phenomenon in a rectangular enclosure heated isothermally at its vertical side.

The first part of this work investigates experimentally the thermophysical characterization of RT27, RT21 and RT35HC including latent heats of melting / solidification and melting/ solidification temperatures, thermal reliability and stability, specific heat capacities, thermal conductivities. These measured thermophysical properties are used input parameters to the numerical simulation. The first aim of this numerical study is to investigate the melting of waxes. This is achieved through an analysis of the heat transfer's regimes and through a parametric study of the Rayleigh number and the aspect ratio effects on the melting process. The second objective is to compare their performance during the melting process under the same boundary conditions. To achieve these goals, the enthalpy-porosity method is employed to describe the physical problem considering the natural convection. The control volume based finite element method CVFEM is used for the spatial discretization. The SIMPLER algorithm is used to solve the pressure -velocity coupling problem. The resulting algebraic system is solved by Tri-Diagonal-Matrix-Algorithm TDMA line by line method.

Preprints (www.preprints.org) | NOT PEER-REVIEWED | Posted: 4 March 2019 doi:10.20944/preprints201903.0034.v1

2. Materials and experimental methods

2.1. Materials

In this project, three paraffins waxes RT27, RT21 and RT35HC were selected. Their thermophysical properties are determined experimentally using the described methods in the following paragraphs. Their specific heats, dynamic viscosities and their thermal expansion coefficients are presented in table 1 [11] [12].

Table 1. Specific heats, viscosities and thermal expansion coefficients of PCMs

Properties	Matter State	RT27 [11]	RT21 [11]	RT35HC [12]
C_p ($J..kg^{-1}.K^{-1}$)	Solid	2400	2100	2000
	Liquid	1800	4200	2000
μ ($kg.m^{-1}s^{-1}$)		3.4210^{-3}	2.810^{-3}	2.710^{-3}
β (K^{-1})		0.510^{-3}	0.510^{-3}	0.7610^{-3}

2.2. Experimental methods

Differential scanning calorimetry

In order to measure the latent heats, melting and solidification temperature of waxes, a differential scanning calorimeter type'' Perkin Elmer model" [13] with a heating rate of 10 °C/min was used. The calorimeter was calibrated in temperature and enthalpy by using the indium as a reference material. The weights of RT27, RT21 and RT35HC are respectively 7.9 mg , 7.82 mg and 7.66 mg with an accuracy of 0.01mg. Cyclic experiments are carried out by 10 heating and 10 cooling at 10 °C/min to study the repeatability of measurements as well as the thermal reliability of paraffins waxes.

DSC measurements are performed also at a heating rate of 10 °C/min to determine the specific heat capacities of the paraffins. In fact, three steps are necessary to calculate C_P for each specimen. First, the baseline, which corresponds to the heat flow signal obtained with both empty crucibles in the DSC furnaces, is measured. Then, a mass of 28.4 mg of sapphire, used as a standard material with known specific heat, is placed in one of the empty crucibles used in the previous step and heated. The heat flow of the sapphire is recorded. In the final step of the specific heat determination, the sapphire is removed from the crucible and replaced by the sample. The sample is heated and its flow signal is measured. Thus, the specific heat capacity of a specimen is determined by the following expression:

$$C_{p,sample}(T) = C_{p,sapphire}(T)\frac{\varphi_{sample}(T)-\varphi_0(T)}{\varphi_{sapphire}(T)-\varphi_0((T)}\frac{m_{sapphire}}{m_{sample}}, \quad (1)$$

Thermogravimetric analysis "TGA"

TGA measurements are investigated using TGA 4000 (Perkin Elmer, USA) at temperature range from 20 °C to 400 °C at a heating rate of 5 °C/min under nitrogen atmosphere. Nitrogen gas was passed through the instrument at a flow rate of 20 ml·min^{-1}. The weights of the samples varied from

Preprints (www.preprints.org) | NOT PEER-REVIEWED | Posted: 4 March 2019 doi:10.20944/preprints201903.0034.v1

10 to 20 mg.

Transient Plane Source

Thermal conductivities of paraffins waxes at solid and liquid states are measured using the transient plane source method "Hot disk" with the TPS 2500 apparatus [14]. This method utilizes a sensor in a shape of double spiral nickel foil covered with a kapton foil to ensure the electric insulation. This sensor acts simultaneously as a heater and a temperature sensor ("Wheatstone bridge"). The sensor is placed in sandwich between two identical solid sample for solid measurements (fig.1) and its totally immersed in the liquid paraffin for the measurements at the liquid state (fig. 2). The accuracy of hot disk results is 5%.

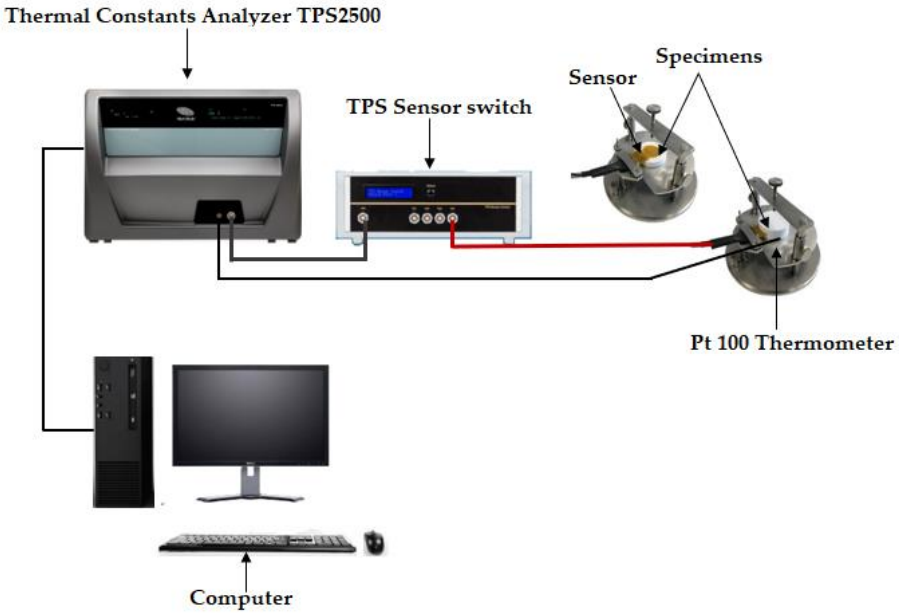

Figure 1. Experimental set-up for measurement at the solid state

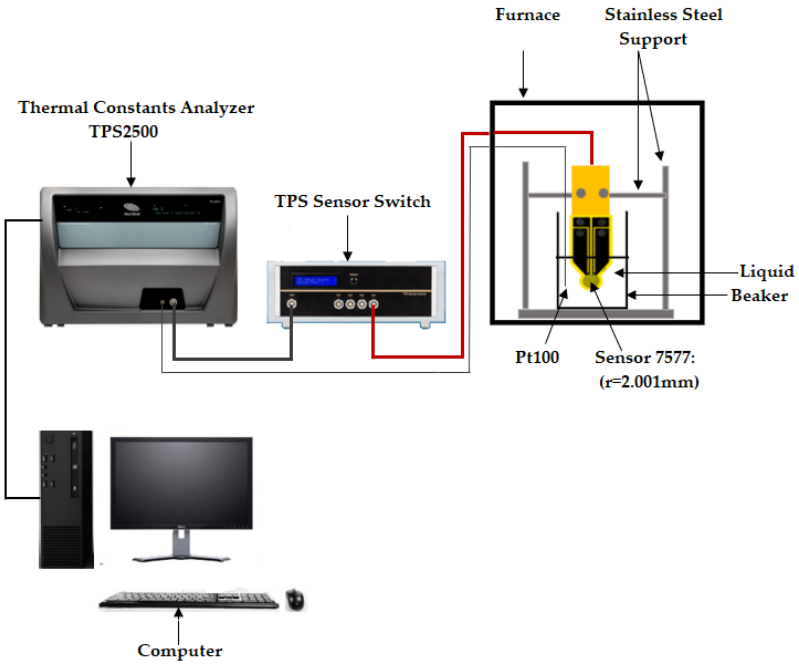

Figure 2. Experimental set-up for measurement at the liquid state

Preprints (www.preprints.org) | NOT PEER-REVIEWED | Posted: 4 March 2019 doi:10.20944/preprints201903.0034.v1

Density measurements

Density of paraffins, defined in equation (2), are examined at the solid and liquid states by pycnometers which consist in glass containers with a volume accurately known thanks to their glass stopper.

$$\rho = \frac{m}{V}, \tag{2}$$

The measurements of the density at the solid state are performed by the following steps. First, the pycnometer, is filled with distilled water with known density. The volume of the water in the pycnometer is determined in equation (3). In the second step , we empty the pycnometer and we dry it carefully. Then, the sample is placed in the pycnometer and the distilled water is added until that reaches the stopper. The volume of this water V'_{H2O} is defined in equation (4). The sample's volume is deduced from equations (3) and (4) and it is presented in equation (5). The density of the sample at the solid state is consequently calculated using the equation (2).

$$V_{H_2O} = \frac{m_{H_2O}}{\rho_{H_2O}}, \tag{3}$$

$$V'_{H_2O} = \frac{m'_{H_2O}}{\rho_{H_2O}} = \frac{m_{pyc-filled} - m_{sample} - m_{pyc-empty}}{\rho_{H_2O}}, \tag{4}$$

$$V_{sample,solid} = V_{H_2O} - V'_{H_2O}, \tag{5}$$

For the density measurements at the liquid state, the pycnometer is filled firstly with distilled water whose volume is defined in equation (3). Then, it is emptied, dried and filled with liquid paraffin until the stopper. The density at the liquid state is obtained by combining equation (1) and (2) since that $V_{sample,liq} = V_{H2O}$. It is described in equation (6)

$$\rho_{sample,liq} = \frac{m_{sample,liq}}{m_{H_2O}} \rho_{H_2O}, \tag{6}$$

3. Mathematical formulation

3.1 Physical problem description

The physical model under investigation is illustrated in **Fig. 3**. It is a rectangular enclosure of width L, height H and aspect ratio $A = \frac{L}{H}$. The enclosure is filled with a PCM initially in the solid state at its melting temperature T_m. At a certain instant of time $t > 0$, the left vertical wall is suddenly heated and thereafter kept at a constant temperature $T_h > T_m$ while the right vertical wall is maintained at a cold constant temperature equal to the melting temperature $T_c = T_m$. The bottom and the upper walls are adiabatic.

Preprints (www.preprints.org) | NOT PEER-REVIEWED | Posted: 4 March 2019 doi:10.20944/preprints201903.0034.v1

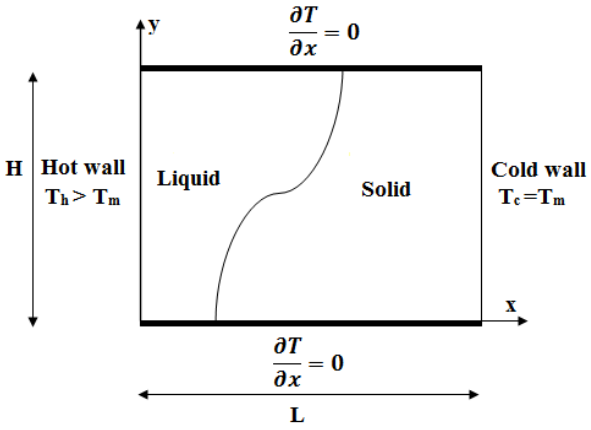

Fig. 3. Schematic illustration of the physical model

3.2 Assumptions

The mathematical formulation of the melting process in a rectangular enclosure requires the following assumptions in order to simplify the physical problem. These assumptions are divided into two groups.

3.2.1 General assumptions

They are related to the geometry of the problem, the flow and the heat transfer:

- The problem is two-dimensional: the depth of the rectangular enclosure is very large compared to its width and its height.
- The physical properties are constant in both solid and liquid phases except for the density which follows the Boussinesq approximation.
- The natural convection is taken into account through the Boussinesq approximation:

  This approximation assumes that the density of the PCM has a constant value in the governing equation except in the terms of the body force in the momentum equation, in which the density, ρ ,varies with the temperature and it takes into account the thermal expansion coefficient, β . It is written in equation (1) where T_0 is the reference temperature at which the reference density ρ_0 is measured. In this study, the reference temperature is taken as the melting temperature $T_0 = T_m$

$$\rho = \rho_0(1-\beta(T-T_0)), \qquad (7)$$

- The flow in the liquid state is laminar.
- The viscous dissipation terms are neglected.
- The fluid is Newtonian and incompressible.
- The heat transfer by radiation is neglected.

3.2.2 Assumptions related to the solid-liquid phase change process

- The physical properties are assumed to be the same in the solid and liquid regions.
- The PCM is perfectly pure: there are no air bubbles in the PCM and the solid-liquid phase change process takes place at a constant temperature.
- The PCM is homogeneous and isotropic.

Preprints (www.preprints.org) | NOT PEER-REVIEWED | Posted: 4 March 2019 doi:10.20944/preprints201903.0034.v1

- The volume variation resulting from the phase change is neglected.

3.3 Governing equations

Based on the above assumptions, the enthalpy-porosity method **[15]** is used to describe the melting of the PCM. In this formulation method, a unique set of governing equations and boundary conditions describes the entire domain: the solid phase, the liquid phase and the mushy zone (where the two phases coexist simultaneously) by the following dimensionless equations:

Continuity equation

$$\frac{\partial U}{\partial X}+\frac{\partial V}{\partial Y}=0, \tag{8}$$

Momentum equation

$$\frac{\partial U}{\partial Fo}+U\frac{\partial U}{\partial X}+V\frac{\partial U}{\partial Y}=Pr\left(\frac{\partial^2 U}{\partial X^2}+\frac{\partial^2 U}{\partial Y^2}\right)-\frac{\partial P}{\partial X}+S_U, \tag{9}$$

$$\frac{\partial V}{\partial Fo}+U\frac{\partial V}{\partial X}+V\frac{\partial V}{\partial Y}=Pr\left(\frac{\partial^2 V}{\partial X^2}+\frac{\partial^2 V}{\partial Y^2}\right)-\frac{\partial P}{\partial Y}+Ra\,Pr\,\theta+S_V, \tag{10}$$

S_U and S_V which was introduced by Voller and Prakash **[16]**, represent the sources terms added to the momentum equations in order to allow the suppression of the velocity field in the solid phase. They are deduced from Karman -Coseney law by the following expressions:

$$S_U=-C_m\frac{1-f_l^2}{q+f_l^3}U,\quad S_V=-C_m\frac{1-f_l^2}{q+f_l^3}V$$

C_m is a mushy zone constant reflecting the morphology of the melting front. It should have a large value to allow the extinction of the velocity field in the solid phase. In fact, in the solid phase, the liquid fraction is null (f_l=0). S_U and S_V tend consequently to infinity. These terms dominate the rest of the terms of the momentum equations and force the velocities to be nulls in order to satisfy the conservation equations conditions. In the liquid phase (f_l =1), S_U and S_V are nulls and the flow is described by the classical Navier-Stokes equations. C_m has usually a value between 10^4 et 10^7.

q is a small constant number introduced to avoid division by zero in the solid phase (f_l=0)

This study is investigated with these parameters [17]: C_m = 1.6 10^6 and q=0.001

Energy equation

$$\frac{\partial\theta}{\partial Fo}+U\frac{\partial\theta}{\partial X}+V\frac{\partial\theta}{\partial Y}=\left(\frac{\partial^2\theta}{\partial X^2}+\frac{\partial^2\theta}{\partial Y^2}\right)-\frac{1}{Ste}\frac{\partial f_l}{\partial Fo}, \tag{11}$$

$\frac{1}{Ste}\frac{\partial f_l}{\partial Fo}$ is the source term related to the phase change.

The liquid fraction f_l can be defined as follows:

f_l = 0 if $\theta < \theta_m$; θ_m is the dimensionless melting temperature of the PCM.

f_l = 1 if $\theta > \theta_m$

The dimensionless variables used in the set of the governing equations are defined below:

$$X=\frac{x}{H},\quad Y=\frac{y}{H},\quad U=\frac{uH}{\alpha},\quad V=\frac{vH}{\alpha},\quad Fo=\frac{\alpha t}{H^2},\quad P=\frac{pH^2}{\rho\alpha^2},\quad \theta=\frac{T-T_m}{T_h-T_c},\alpha=\frac{\lambda}{\rho C_p}$$

Preprints (www.preprints.org) | NOT PEER-REVIEWED | Posted: 4 March 2019 doi:10.20944/preprints201903.0034.v1

The studied problem is governed by the following dimensionless parameters:

The Prandtl number $\mathrm{Pr} = \frac{\nu}{\alpha} = \frac{\mu C_p}{\lambda}$

The Rayleigh number $\mathrm{Ra} = \frac{g\beta(T_h - T_c)H^3}{\nu\alpha}$

The Stefan number $\mathrm{Ste} = \frac{C_p(T_h - T_m)}{L_H}$

3.4 Initial and boundaries conditions

At Fo = 0: U=V=θ=0

At the left vertical wall X=0, Y ∈ [0,1]: θ=1, U=0 , V=0 ∀ Fo > 0,

At the right vertical wall $X = \frac{L}{H}$, Y∈ [0,1]: θ=0, U=0 , V=0 ∀ Fo > 0

At the horizontal bottom wall X∈ $[0, \frac{L}{H}]$: $Y = 0$: $\frac{\partial\theta}{\partial Y}$ = 0 (adiabatic wall), U=0 , V=0 ∀ Fo > 0

At the horizontal upper wall X∈ $[0, \frac{L}{H}]$: $Y = 1$: $\frac{\partial\theta}{\partial Y}$ = 0 (adiabatic wall), U=0 , V=0 ∀ Fo > 0

4. Numerical procedure

Numerical simulations are carried out using a Fortran program. This program uses the control volume based element method (CVFEM) **[17-19]** for the spatial discretization and the implicit scheme for the time discretization. The SIMPLER algorithm is used in this program to solve the pressure - velocity coupling problem. The resulting algebraic system is solved by Tri-Diagonal- Matrix-Algorithm TDMA line by line method.

The energy equation contains the dimensionless temperature and the liquid fraction as unknown variables. That's why, it is necessary to have an equation for the liquid fraction update to solve the problem. According to the Brent formulation **[15, 17, 20]**, the liquid fraction is updated at each iteration using the following expression:

$$f_{lij}^{\,n+1} = f_{lij}^{\,n} + w\mathrm{Ste}\frac{\Delta Fo}{V_{ij}} a_{ij}\left(\theta_{ij}^{n} - \theta_{m}\right), \qquad (12)$$

Where n, n+1 refers to the iterations levels, w is the relaxation coefficient, ΔFo is the dimensionless step time, V_{ij} is the control volume around a node ij, a_{ij} is the discretized energy coefficient. After each update, the liquid fraction is submitted to the following correction: $f_{lij} = 1$ if $f_{lij} > 1$.

5. Results and discussions

5.1 Thermophysical properties of paraffins

5.1.1 DSC Analysis

Paraffins RT27, RT21 and RT35HC are submitted to ten successive thermal cycles. Their DSC curves of the second thermal cycle are illustrated and analyzed in the figures 4-9. It can be seen from figures 4,5,6 and 7 that the DSC curves of RT27 and RT21 have two peaks. The major peak is attributed to the solid-liquid phase change during the heating process and to the liquid-solid phase change

Preprints (www.preprints.org) | NOT PEER-REVIEWED | Posted: 4 March 2019 doi:10.20944/preprints201903.0034.v1

during the cooling process. Results show that the latent heats of melting of RT27 and RT21 are respectively 146.796 J/g and 123.829 J/g with a melting temperature of 25.15°C and 18.24° . The latent heats of solidification of RT27 and RT21 are respectively 146.139 J/g and 130.125 J/g and their solidification temperatures are respectively 24.25°C and 20,71°C. The difference observed between the melting and solidification temperatures of these paraffins is due to the supercooling phenomenon. In fact, the comparison of the behavior of RT27 and RT21 show that the degree of supercooling of RT27 is 0.9 °C whereas it is 2.47°C for RT21. This difference between the supercololing intensity of RT27 and RT21 can be related to a difference in the intermolecular hydrogen bonding between molecules [21]. The minor peaks of the DSC curves' RT27 and RT21 concern the solid-solid phase change. The inspection of figures 4, 5, 6 and 7 reveals that the latent heats of the solid-solid phase change of RT27 and RT21 are respectively 19.63 J/g and 8.3 J/g during the heating process and they are of 19.01 J/g and 7.078 during the cooling process.

Besides, figures 8 and 9 show that RT35HC has only one pic during the heating and cooling process. This peak corresponds to the heat absorbed during the solid-liquid phase change which is of 211.53 J/g with a melting temperature of 35.82°C and to the heat released during the liquid-solid phase change which is of 208.48 J/g with a solidification temperature of 32.20°C . The absence of the minor peak of the solid-solid transition in the DSC curves of RT35HC can be related to the molecular length and to the composition of n-alkanes C_nH_{2n+2} forming the paraffin wax. In fact, it was reported in [22-24] that n-alkanes with n inferior than 20 and paraffin molecules with n lower than 50 have only one pic which corresponds to the solid-liquid phase change and they don't present a solid-solid transition .

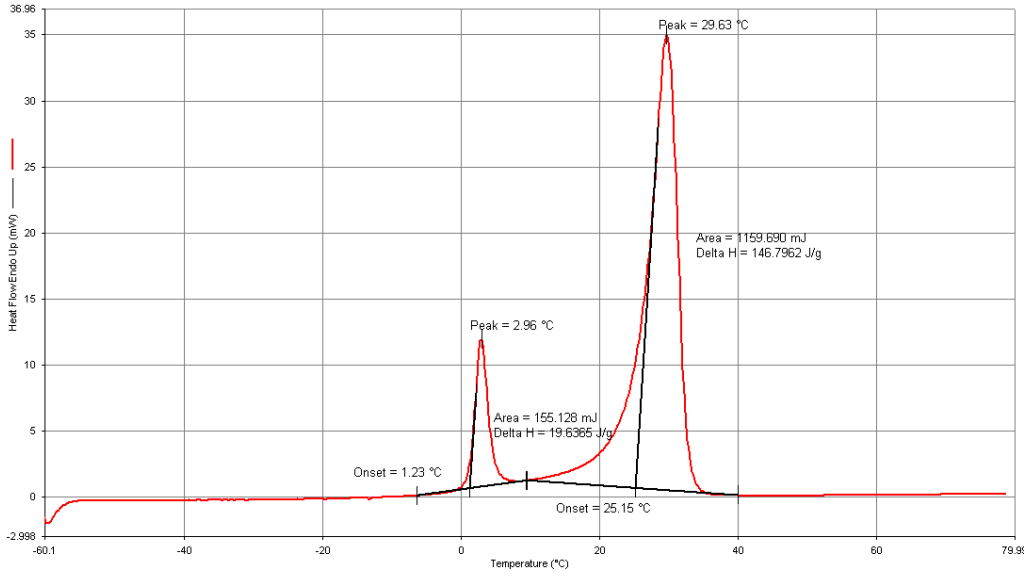

Fig. 4. DSC curve for the heating of RT27

Preprints (www.preprints.org) | NOT PEER-REVIEWED | Posted: 4 March 2019 doi:10.20944/preprints201903.0034.v1

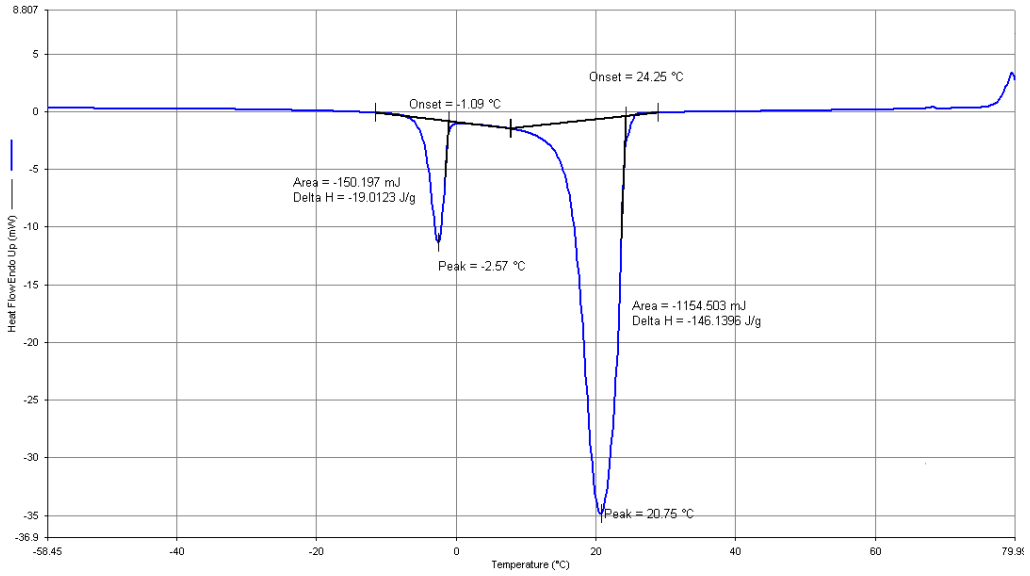

Fig. 5. DSC curve for the cooling of RT27

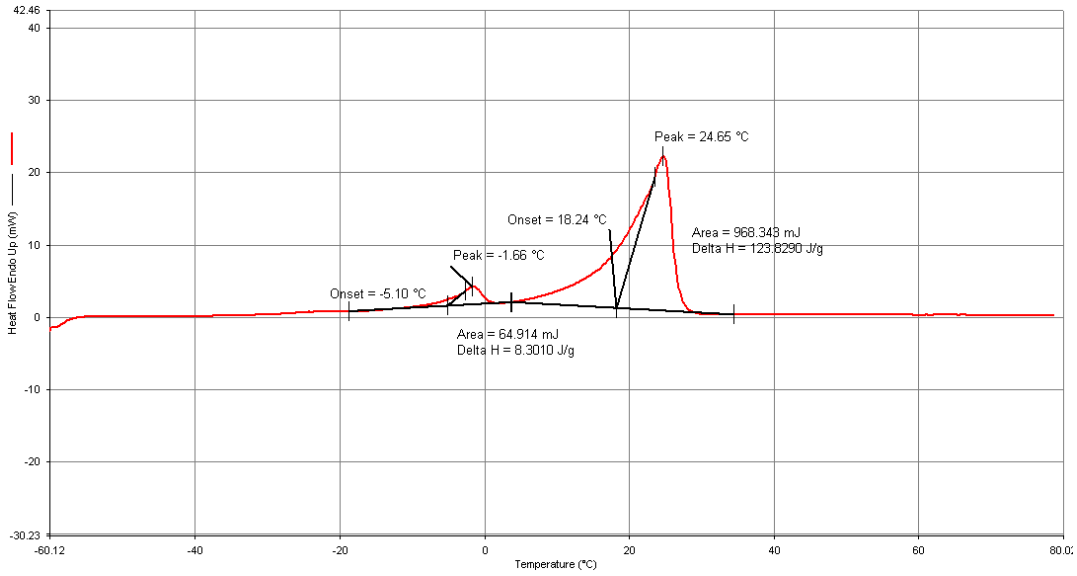

Fig. 6. DSC curve for the heating of RT21

Preprints (www.preprints.org) | NOT PEER-REVIEWED | Posted: 4 March 2019 doi:10.20944/preprints201903.0034.v1

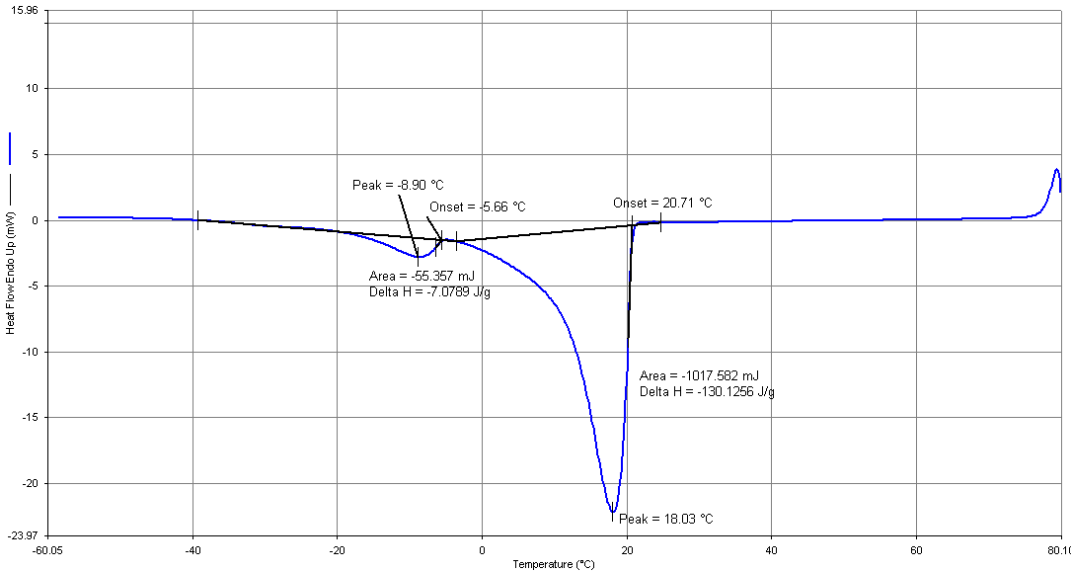

Fig. 7. DSC curve for the cooling of RT21

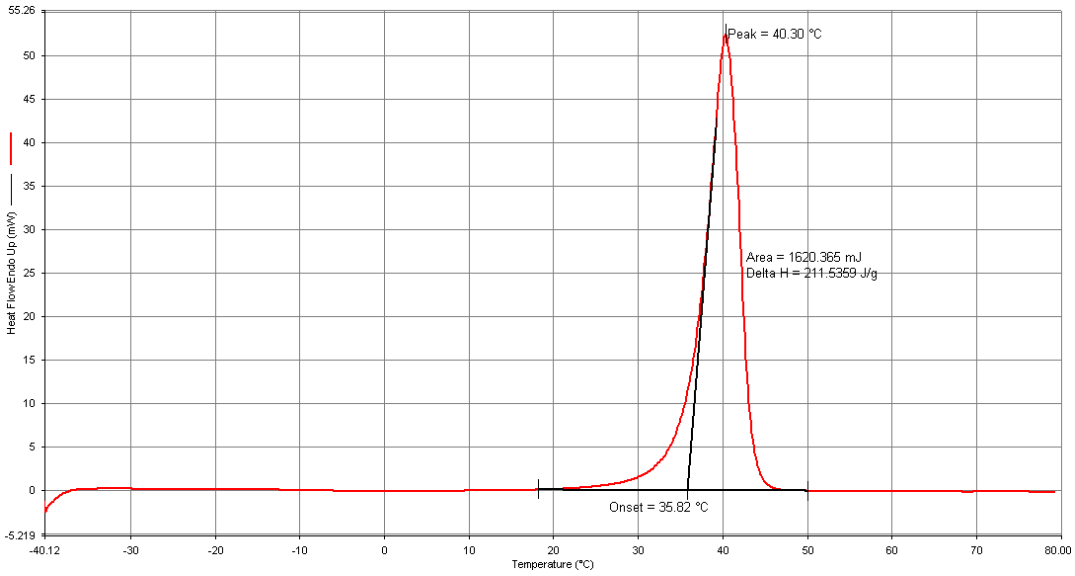

Fig. 8. DSC curve for the heating of RT35HC

Preprints (www.preprints.org) | NOT PEER-REVIEWED | Posted: 4 March 2019 doi:10.20944/preprints201903.0034.v1

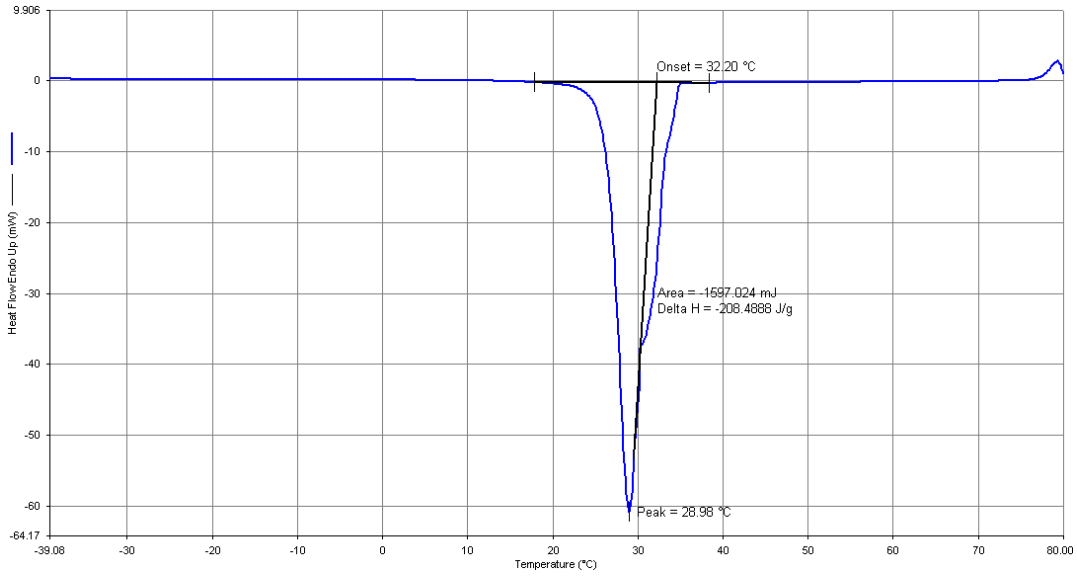

Fig. 9. DSC curve for the cooling of RT35HC

The ten thermal cycles are analyzed and average values of DSC results for each paraffin are summarized in table 2.

Table 2. Phase change properties of RT27, RT21 and RT35HC

	Heating				**Cooling**			
	Solid-Solid		**Solid-Liquid**		**Liquid-Solid**		**Solid-Solid**	
	T (˚C)	ΔH(J/g)	T (˚C)	ΔH(J/g)	T (˚C)	ΔH(J/g)	T (˚C)	ΔH(J/g)
RT27	1.50	19.961	25.33	148.198	24.37	145.960	-0.9	18.252
RT21	-5.19	8.8023	18.126	126.839	20.70	129.757	-5.65	7.183
RT35HC	-	-	35.84	211.943	30.173	209.783	-	-

The study of the thermal reliability of paraffins during ten thermal cycles is illustrated in figures

Preprints (www.preprints.org) | NOT PEER-REVIEWED | Posted: 4 March 2019 doi:10.20944/preprints201903.0034.v1

10, 11 and 12. The results show that the DSC curves of RT27 and RT21 and RT35HC during the heating and cooling process are overlaid for each paraffin. In fact, the analyze of the results reveals that the higher variation of the latent heat of melting of RT27, RT21 and RT35HC during the cycles are respectively 3.32 J/g, 3.37 J/g, 1.867 J/g. The greater variation of their latent heat of solidification depicted within the cycles are respectively 2.376 J/g, 1.05 J/g, 3.226 J/g. The examination of the results reveals that the maximum variation of the melting temperature during the ten cycles is 0. 22 °C for RT27, 0.15 for RT21 and 0.04 for RT35HC. The maximum discrepancy between the solidification temperatures during the cycles is 0.19°C for RT27, 0.01 °C for RT21 and 3.96 °C for RT35HC. Thus, the findings of the results' analyzes show that RT27, RT21 and RT35HC are stable over the ten thermal cycles.

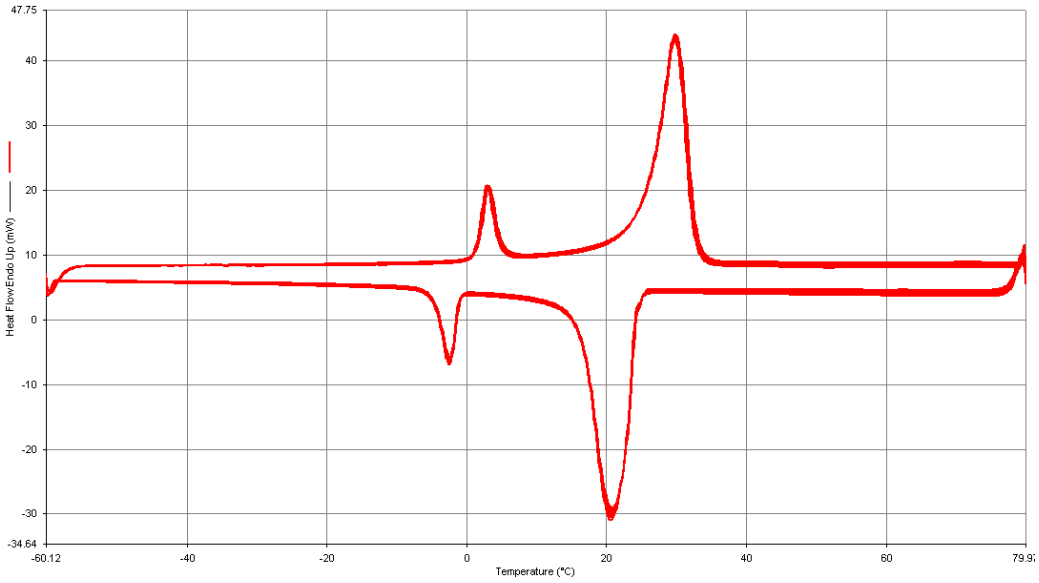

Fig. 10. Thermal cycles of RT27

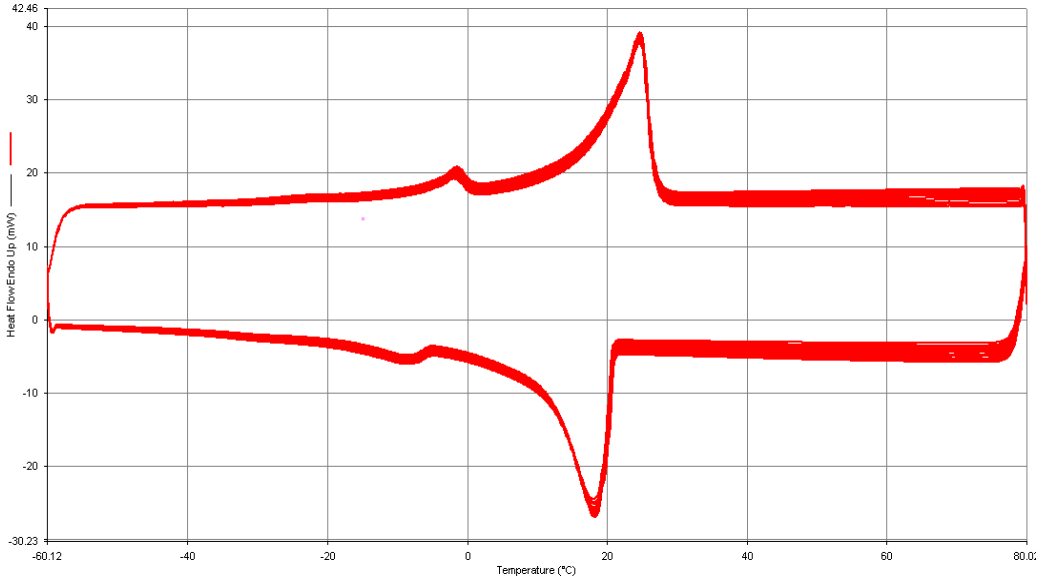

Fig. 11. Thermal cycles of RT21

Preprints (www.preprints.org) | NOT PEER-REVIEWED | Posted: 4 March 2019 doi:10.20944/preprints201903.0034.v1

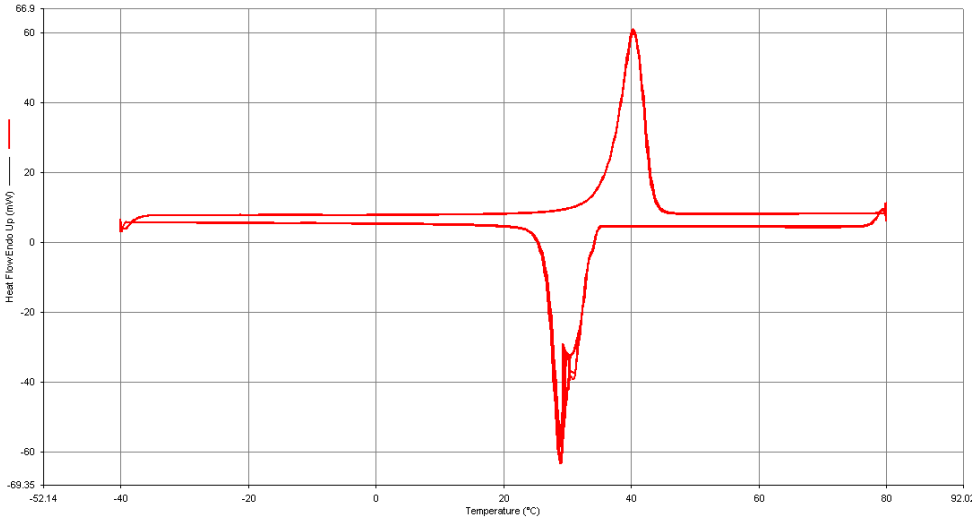

Fig. 12. Thermal cycles of RT35HC

The evolution of the specific heat capacities of RT27, RT21, and RT35HC with temperature are depicted in figures 13-18. Results show that the specific heat capacity increases with temperature in the solid and liquid phases. The experimental results of these figures are fitted to a polynomial temperature dependence described in equation (13). The parameters a, b, c, d and e of the fittings for the three paraffins are displayed in table 3.

$$C_P = aT^4 + bT^3 + cT^2 + dT + e\,, \tag{13}$$

Table 3. Parameters a-e of the fitting of experimental specific heat capacities of RT27, RT21 and RT35HC

	RT27		**RT21**		**RT35HC**	
	Solid	Liquid	Solid	Liquid	Solid	Liquid
a	-0.004	-0.020	-0.021	-0.0009	$-7\ 10^{-5}$	0.0023
b	-0.246	-3.627	-2.673	-0.1535	0.0093	-0.5422
c	-4.836	244.1	-122.5	10.291	0.1933	48.026
d	-17.06	-7288	-2399	-302.45	7.5103	-1876.4
e	1792.8	83442	-15030	2086.5	1542.8	29319

The average specific heat capacity in the solid and liquid phases of RT27, RT21 and RT35HC are summarized in table 4. The comparison between the average specific heat capacity in the solid phase of the three paraffins reveals that the greater C_p is attributed to RT27 which is of 1704,98 J/kg.K whereas the average specific heat capacities of RT21 and RT35HC in the solid phase are respectively 1581.825 J/kg.K and 1569.35 J/kg.K. Concerning the liquid phase, it can be seen that the average specific heat of RT27, RT21 and RT35HC are respectively 1960.137 J/kg.K, 1839.147 J/kg.K and 2000.349 J/kg.K which show that the higher specific heat capacity in the liquid phase is associated to RT35 HC. The comparison between the experimental results of the specific heat capacity of paraffins and the literature data [11-12], illustrated in table 4, show that the deviation of the experimental data of the specific heat capacity in the solid phase of RT27,RT21 and RT35HC are respectively 28.98%, 24.67%, 21.53%. The variation of the specific heat capacity in the liquid phase of paraffins from the literature data are 8.89% for RT27, 56.21% RT21 and 0.017% RT35HC. The reasons of the deviation observed between the experimental results of the specific heat capacity and the literature data [11-12]

Preprints (www.preprints.org) | NOT PEER-REVIEWED | Posted: 4 March 2019 doi:10.20944/preprints201903.0034.v1

can be attributed to the difference between the mass of paraffin used in the DSC measurements and to heating rate.

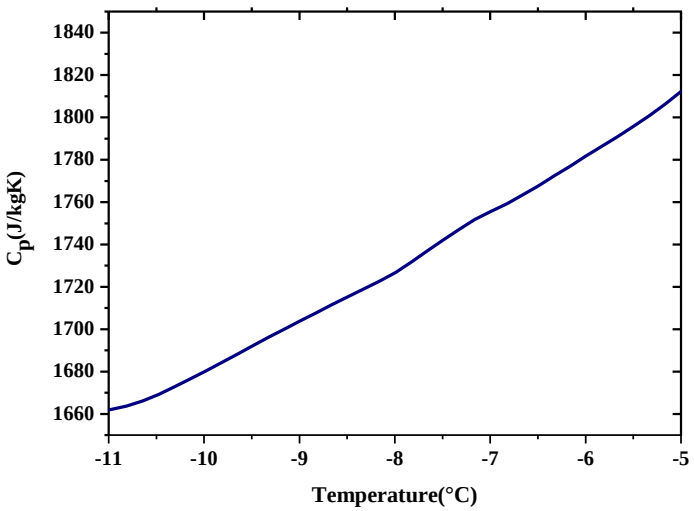

Fig. 13. Evolution of the specific heat capacity of RT27 with temperature in the solid phase

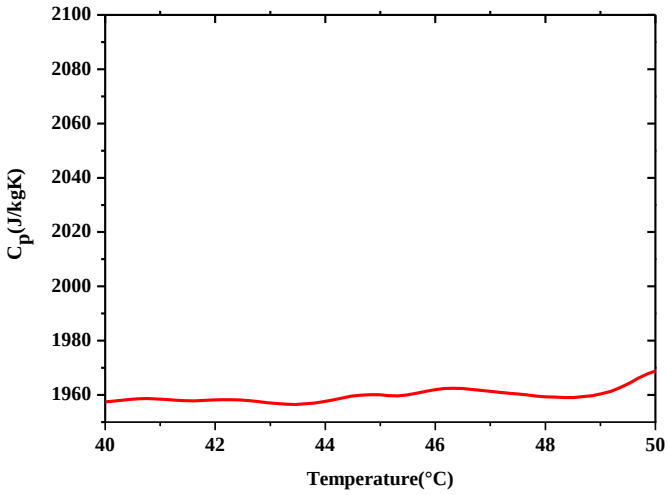

Fig. 14. Evolution of the specific heat capacity of RT27 with temperature in the liquid phase

Preprints (www.preprints.org) | NOT PEER-REVIEWED | Posted: 4 March 2019 doi:10.20944/preprints201903.0034.v1

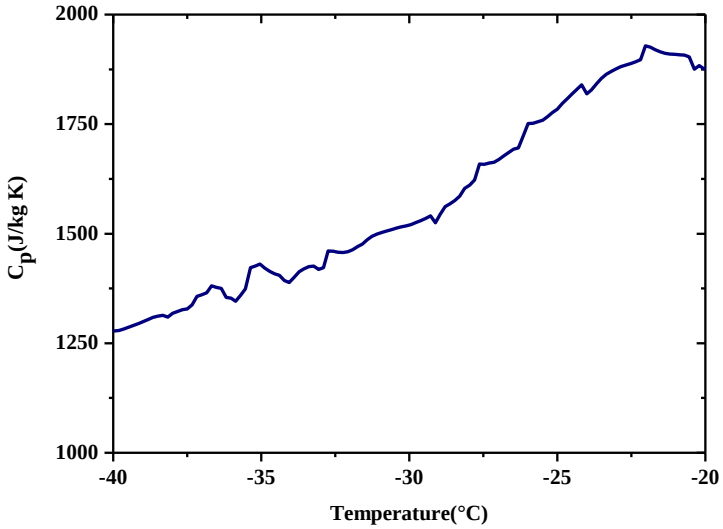

Fig. 15. Evolution of the specific heat capacity of RT21 with temperature in the solid phase

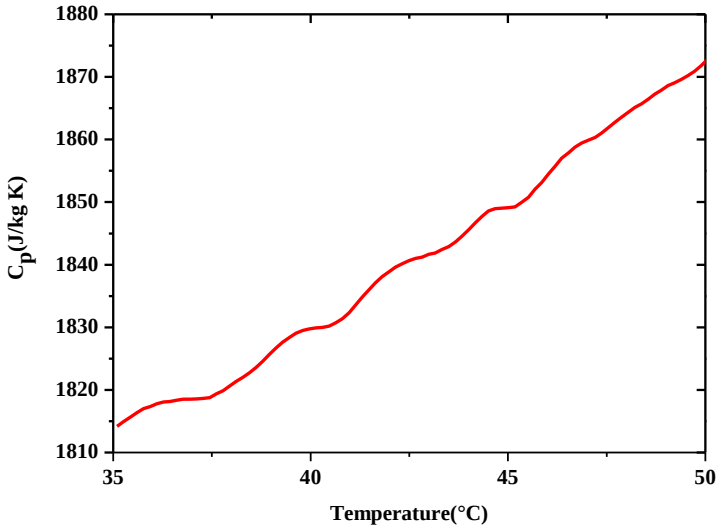

Fig. 16. Evolution of the specific heat capacity of RT21 with temperature in the liquid phase

Preprints (www.preprints.org) | NOT PEER-REVIEWED | Posted: 4 March 2019 doi:10.20944/preprints201903.0034.v1

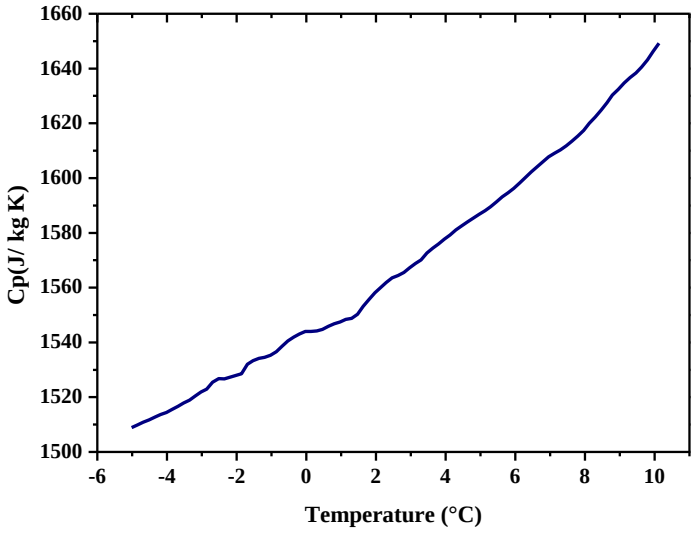

Fig. 17. Evolution of the specific heat capacity of RT35HC with temperature in the solid phase

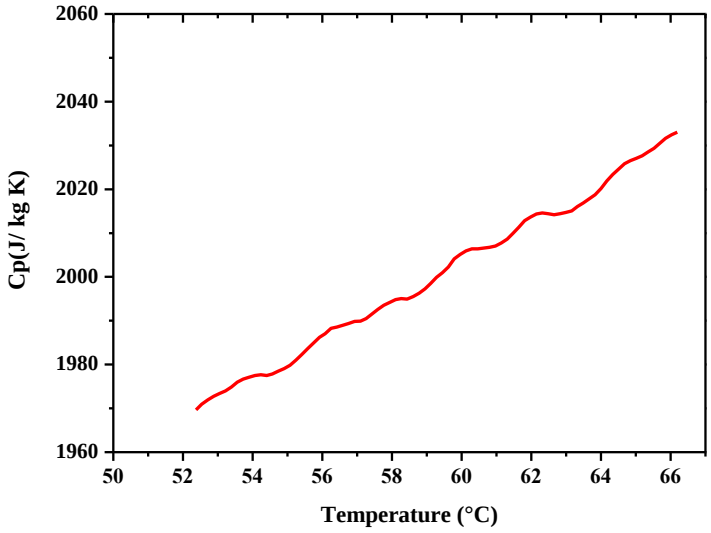

Fig. 18. Evolution of the specific heat capacity of RT35HC with temperature in the liquid phase

Table 4. Comparison between average experimental specific heat capacities and literature's data

	Experimental		Literature	
	C_{psolid} J/kg K	$C_{pliquid}$ J/kg K	C_{psolid} J/kg K	$C_{pliquid}$ J/kg K
RT27	1704.98	1960.137	2400	1800
RT21	1581.825	1839.147	2100	4200
RT35HC	1569.35	2000.349	2000	2000

Preprints (www.preprints.org) | NOT PEER-REVIEWED | Posted: 4 March 2019 doi:10.20944/preprints201903.0034.v1

5.1.2Thermal stability

TGA measurements are performed to study the thermal stability of paraffins. The weight losses of RT27, RT21 and RT35HC are illustrated in figure 19 . It can be seen that the weight losses are negligible (inferior than 2%) for temperature lower than 123 °C for RT27,109 °C for RT21 and 135,4 °C for RT35HC. Then, a rapid increase in the rate of the mass degradations of paraffins is observed until the total degradation of RT27, RT21 and RT35HC is reached respectively at 243 °C, 236 °C,247 °C. As a conclusion, RT27, RT21 and RT35HC are stable over the temperature range of the low temperature thermal storage systems.

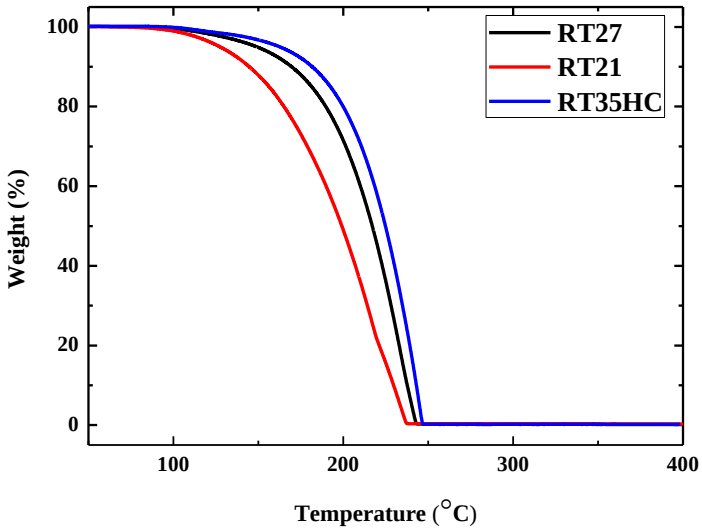

Fig. 19. Thermal degradation of paraffins RT27, RT21 and RT35HC

5.1.3Thermal conductivities

Thermal conductivities of solid and liquid paraffins are summarized in table 5. Results reveal that the thermal conductivity at the solid state is higher than that at the liquid state. The difference between thermal conductivity of the solid and liquid paraffins ($\Delta\lambda = \lambda_s - \lambda_l$) is 0.0468W.m^{-1}.K^{-1}, 0.0718 W.m^{-1}.K^{-1} and 0.1474 W.m^{-1}.K^{-1} respectively for RT27, RT21 and RT35HC. It can be seen also that RT35HC has the highest thermal conductivity compared to RT27 and RT21.

Table 5 . Thermal Conductivities of RT27, RT2DE1 and RT35HC in solid and liquid phases

	λ_s	λ_l
	W.m^{-1}.K^{-1}	**W.m^{-1}.K^{-}**
RT27	0.2345	0.1877
RT21	0.2566	0.1848
RT35HC	0.3341	0.1867

5.1.4Density measurements

The densities of solid and liquid paraffins RT27, RT21 and RT35 HC are presented in table 6. It can be seen that RT35HC has the highest density in the solid and liquid states.

Preprints (www.preprints.org) | NOT PEER-REVIEWED | Posted: 4 March 2019 doi:10.20944/preprints201903.0034.v1

Table 6. Density of RT27, RT21 and RT35HC in solid and liquid phases

	ρ_s	ρ_l
	kg.m^{-3}	kg.m^{-3}
RT27	786.93	785.2
RT21	748.263	729.957
RT35HC	906.362	796.991

5.2 Numerical Analysis of the melting of RT27

5.2.1 Heat transfer characteristics

The study of the melting of the paraffin RT27 in a rectangular enclosure heated isothermally at its left wall is conducted by using a mesh grid of 121 X 121 and a dimensionless step time of $2\ 10^{-5}$. The dimensionless parameters governing this study are: $\boldsymbol{A} = L/H = \mathbf{1}$, $\mathrm{Pr} = 41.04$, $\mathrm{Ra} = 5\ \ 10^{6}$ and $\mathrm{Ste} = 0.04$.

- **Solid-liquid interface evolution**

Fig. 20 illustrates the solid - liquid interface evolution with time during the melting process. The red and blue areas represent the liquid and the solid phases of PCM, respectively. At the beginning of the melting process, it can be observed that a thin layer of liquid PCM is formed and is parallel to the hot wall which implies that conduction is the dominant heat transfer mode. This is due to the fact that the motion of the liquid PCM is hampered by the viscous forces. During this stage, the solid-liquid interface is flat and parallel to the hot wall (**Fig. 20a)**. As time elapses, the liquid layer thickness increases. The buoyancy forces become strong enough to overcome the viscous forces which leads to a development of a growing convection current in the top part of the enclosure. This causes a tilt of the melt front in this part. In the bottom part of the enclosure, the solid-liquid interface remains parallel to the hot wall which proves that conduction is the heat transfer mode in this part **(Fig. 20b**). Thus, the heat transfer is a combination of the natural convection in the top part and the conduction in the bottom part of the enclosure. This corresponds to a transition regime. As time progresses, a continuous increase in the liquid layer thickness is noticed. The effect of the natural convection in the liquid PCM becomes more significant. In fact, during this stage, the solid-liquid interface has an oblique shape. It becomes more distorted as the fluid motion is intensified. It presents tilts in the top and bottom parts of the enclosure indicating that the natural convection is the dominant heat transfer mode **(Fig. 20c–20d**). At later times, the melting front reaches the cold wall in the top part while its tilt increases in the lower part as the PCM continue to melt **(Fig. 20e-20f).**

Preprints (www.preprints.org) | NOT PEER-REVIEWED | Posted: 4 March 2019 doi:10.20944/preprints201903.0034.v1

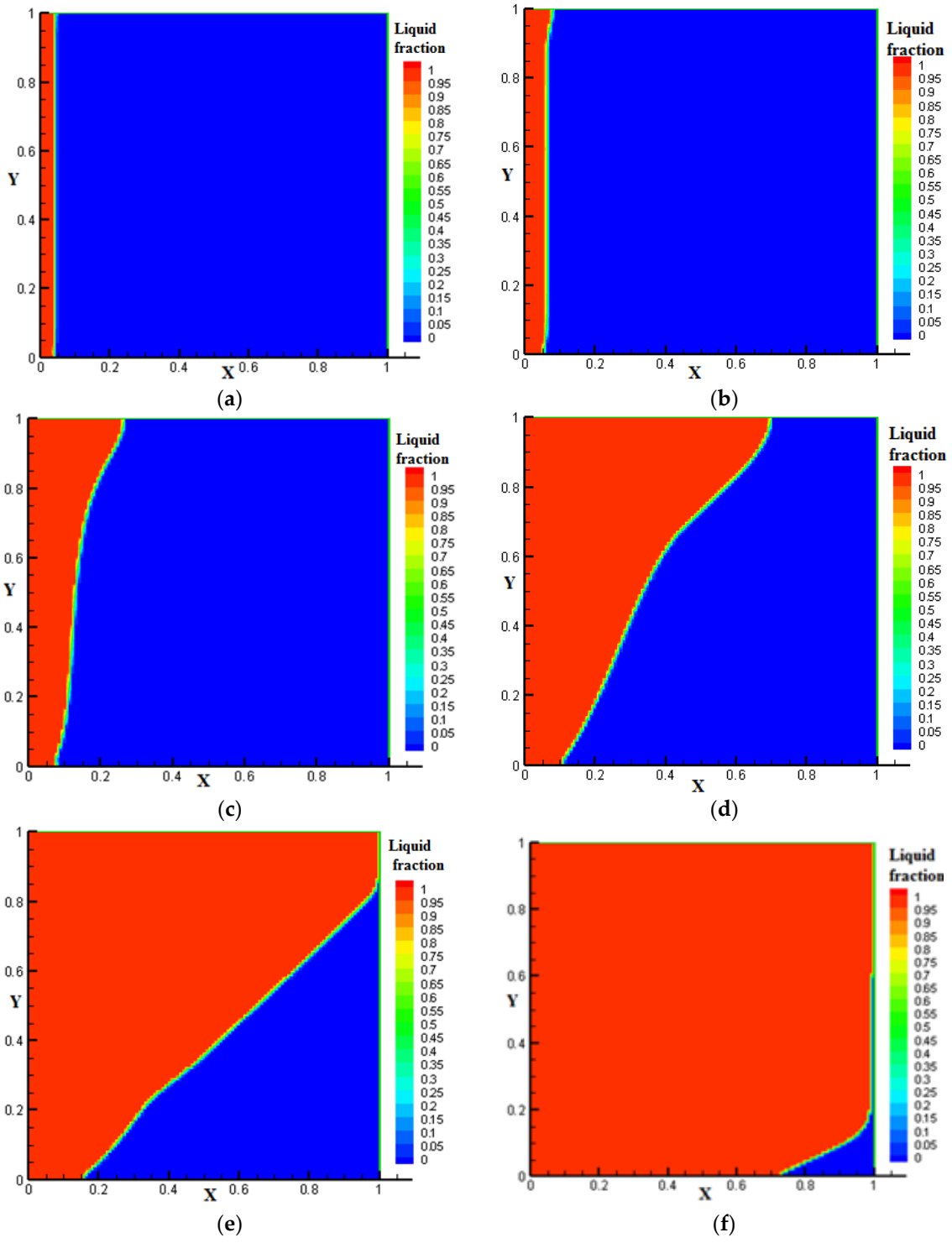

Fig. 20. Time evolution of the solid-liquid interface at (a) FoSte = 0.0008 ; (b) FoSte = 0.004 ; (c) FoSte = 0.008 ; (d) FoSte = 0.024 ; (e) FoSte = 0.06 ; (f) FoSte = 0.12

- **Temperature field evolution**

Fig. 21. displays the temperature contours in the PCM at different dimensionless times. At early times, temperature contours are verticals and parallels to the hot wall which indicates that at this stage the heat transfer mechanism is dominated by conduction **(Fig. 21a).** As time progresses, the temperature of the liquid PCM near the hot wall increases enough so that buoyancy forces overcome the resistance imposed by viscos forces. Consequently, the hot PCM go up along the vertical hot wall and hits the top part of the enclosure. Then, it is deflected and it drops along the solid-liquid interface.

Preprints (www.preprints.org) | NOT PEER-REVIEWED | Posted: 4 March 2019 doi:10.20944/preprints201903.0034.v1

Its temperature decreases as it descends. The deviation of the PCM induces a tilt of temperature contours in the upper part of the enclosure which explains the deformation observed in the isotherms in (**Fig. 21b-21f).**

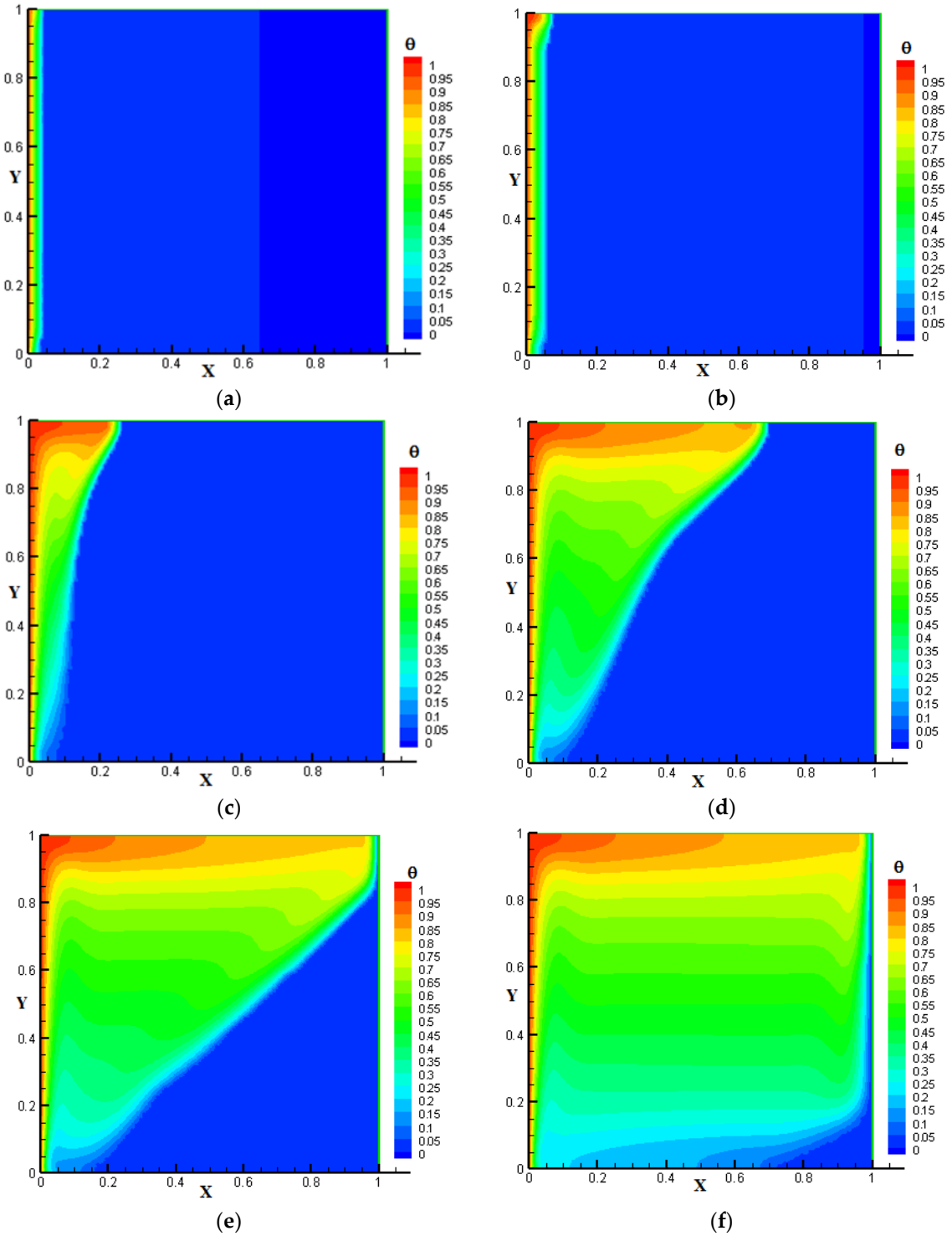

Fig. 21. Isotherms at different dimensionless time (a) FoSte = 0.0008 ; (b) FoSte = 0.004 ; (c) FoSte = 0.008 ; (d) FoSte = 0.024 ; (e) FoSte = 0.06 ; (f) FoSte = 0.12

- **Nusselt number**

The average Nusselt number along the hot vertical wall is defined in equation (14) **[25]**:

Preprints (www.preprints.org) | NOT PEER-REVIEWED | Posted: 4 March 2019 doi:10.20944/preprints201903.0034.v1

$$Nu_h = -\int_0^1 (\frac{\partial \theta}{\partial X})_{X=0} dY \,, \tag{14}$$

Its temporal variation illustrated in **Fig. 22** is exploited to analyze the heat transfer mechanisms within the melting process. In fact, it can be observed from **Fig. 22a and Fig. 22b** that at the beginning of the melting of the PCM, the Nusselt number has a relatively high magnitude then it decreases rapidly. This drop reveals that at this stage, the heat transfer rate decreases as the melt layer increases. This indicates that the first regime of heat transfer during the melting process is the conduction regime. The initial high value of Nusselt number is due to the small thermal resistance of the thin liquid layer in the vicinity of the hot wall which gives rise to the heat transfer rate at early times of the melting leading to a large value of Nusselt number. The end of the conduction regime is announced by the minimum value observed in the Nusselt number. Then, Nu_h rises slightly during a short period which indicates an increase in the heat transfer rate caused by the formation of the natural convection current. This corresponds to the transition regime where both conduction and natural convection are the heat transfer mechanisms controlling the melting process. Then, the Nusselt number displays a quasi steady state value representing the dominant natural convection regime. At later times, Nu_h shows a slight decrease indicating that the effect of the natural convection decreases at this stage comparing to the previous times. This regime appears when the solid-liquid interface attains the opposite wall **(Fig. 20e- 20f**). It is caused by the decrease of the length of the melting front as the solid PCM continue to shrink. The link between the length of the solid-liquid interface and the intensity of the natural convection is due to the fact that the interface represents the cold source in the formation of the natural convection currents. Thus, the diminution of its length reduces the strength of the natural convection which leads to the slight drop observed on the Nusselt number. It is important to mention that despite the decrease of the effect of the natural convection at this stage, the heat transfer regime remains always the convection regime.

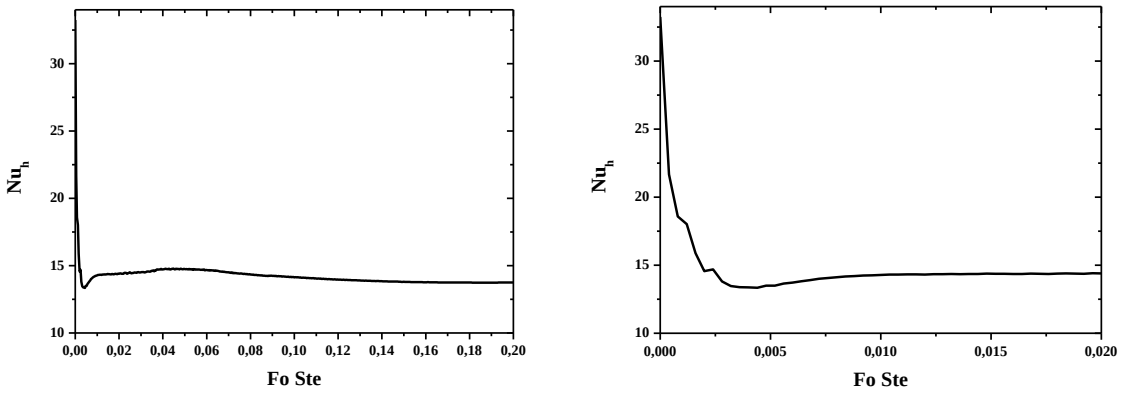

Figure 22. (a) Temporal variations of the average Nusselt number along the hot wall during the melting of RT27; (b) Detailed illustration of the temporal variations of the average Nusselt number along the hot wall until $FoSte = 0.02$

- **Melting rate**

The melt fraction is defined as the ratio of the molten volume of PCM and the total volume of PCM. It is expressed in equation (15) where f_{lij} represents the liquid fraction in the control volume V_{ij} around a node (i, j).

Preprints (www.preprints.org) | NOT PEER-REVIEWED | Posted: 4 March 2019 doi:10.20944/preprints201903.0034.v1

$$\gamma = \frac{V_{molten}}{V_{PCM}} = \frac{1}{LH}\sum f_{ij} V_{ij}\,, \tag{15}$$

Fig. 23. illustrates the time evolution of the melt fraction of RT27 during its melting process. It can be shown from this figure that the melt fraction rises linearly with time until $Fo\ Ste = 0.06$. At this stage, 80%of the initial solid RT27 is molten. Then, the melt fraction evolution becomes gradually curved which indicates a decrease in the melting rate comparing to the previous stage. This decrease is due to the diminution of the strength of the natural convection in the liquid PCM from the moment the solid-liquid interface reaches the opposite wall of the enclosure within the melting process. A detailed explanation of the reason's decrease of the natural convection strength was presented in the previous paragraph (Nusselt Number).

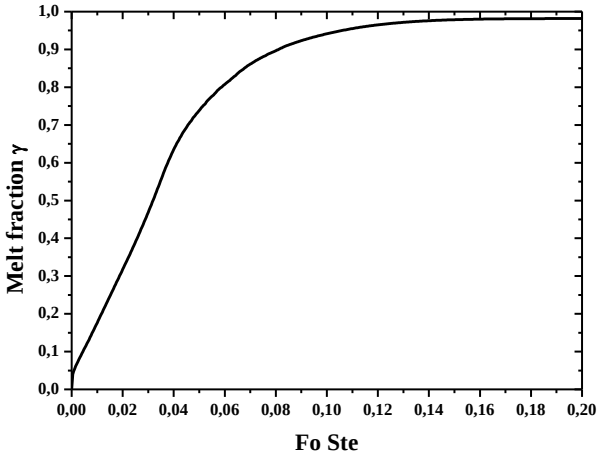

Fig. 23. Time evolution of melt fraction of RT27

5.2.2 *Parametric study*

- **Effect of the Rayleigh number**

Fig. 24 shows the time evolution of the melt fraction of RT27 for different Rayleigh numbers. It can be seen from this figure that the PCM melts more rapidly as the Ra increases. This is due to the fact that higher Ra means stronger natural convection which enhances the heat transfer. For a deep understanding of the effect of this number on the heat transfer mechanism within the melting phenomenon, the temporal variation of the average Nusselt number along the hot vertical wall Nu_h illustrated in **Fig. 25** for different Ra is used. It is inferred from this figure **(Fig.25a and Fig.25b)** that the minimum value of Nu_h is reached earlier as Ra increases. This implies that the rise of the Ra reduces the period of the conduction dominated regime and advances the development of the natural convection currents in the liquid PCM. Careful examination in **Fig. 25** indicates also that among the Ra used in this study, the highest value of the quasi-steady Nu_h is attributed to the $Ra = 5\ 10^6$. Then, it decreases as the Ra decreases. This result proves that the intensity of the natural convection is more important as the Ra is higher.

Preprints (www.preprints.org) | NOT PEER-REVIEWED | Posted: 4 March 2019 doi:10.20944/preprints201903.0034.v1

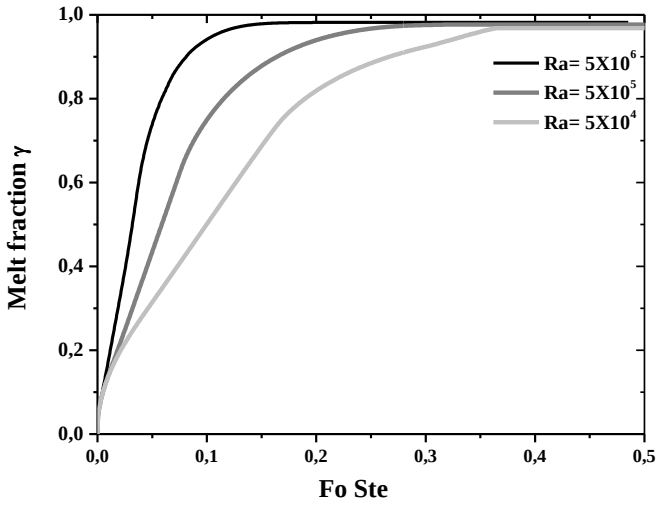

Fig. 24. Effect of Rayleigh number on the time evolution of the melt fraction for: $Pr = 41.04$, $Ste = 0.04$, $A = 1$

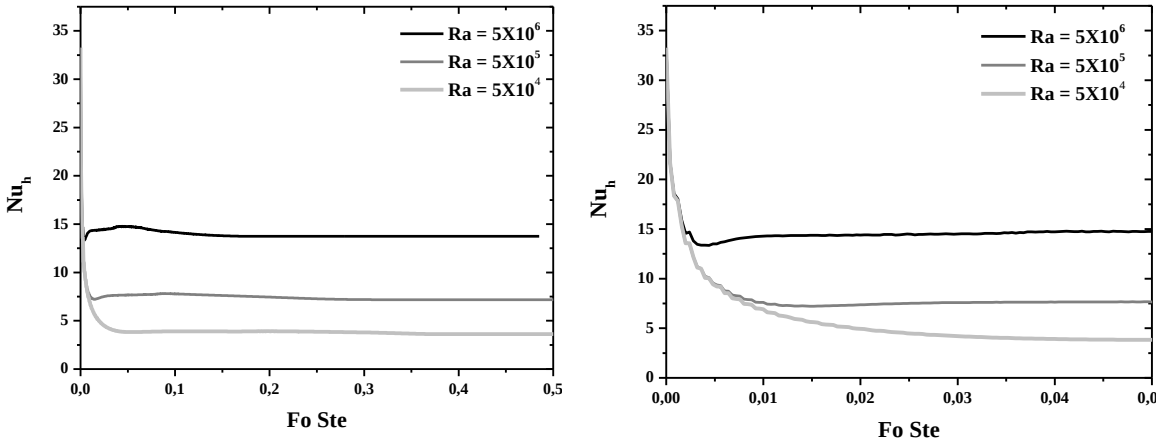

Fig. 25. (a) Effect of Rayleigh number on the temporal variations of the average Nusselt number along the hot wall for $Pr = 41.04$, $Ste = 0.04$, $A = 1$; (b) Detailed illustration of the effect of Rayleigh number on the temporal variations of Nusselt number until $FoSte = 0.05$

- **Effect of the aspect ratio A**

The time evolution of the melt fraction for three different aspect ratios $A = \frac{L}{H}$ (various widths are used while the height remains constant) of the enclosure are presented in **Fig. 26**. It can be clearly observed from this figure that the melting process is faster as the aspect ratio is smaller. The explanation of this result is carried out through the understanding of the effect of A on the temporal variation of the average Nusselt number along the hot vertical wall which is displayed in **Fig. 27.** Inspection of this figure discloses that the value of the quasi-steady Nu_h is higher as the aspect ratio A is smaller. This reflects that the effect of the natural convection in the liquid PCM is more significant in the enclosure with smaller A. Hence, the decreasing of A leads to an enhancement of the heat transfer rate during the melting process. Consequently, this phenomenon becomes more rapid as the two verticals walls are closer.

Preprints (www.preprints.org) | NOT PEER-REVIEWED | Posted: 4 March 2019 doi:10.20944/preprints201903.0034.v1

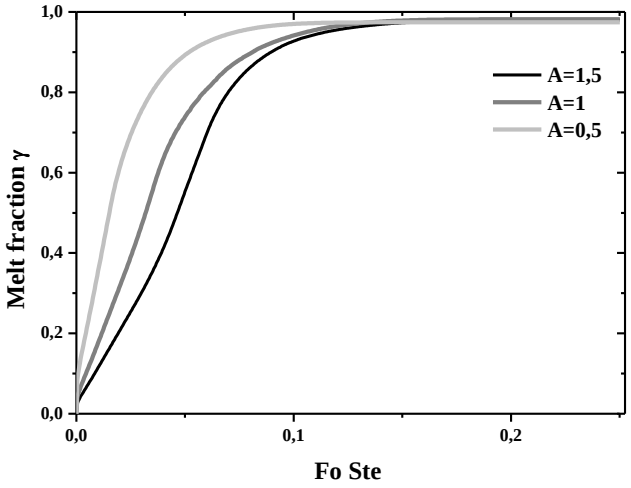

Fig. 26. Effect of the aspect ratio on the time evolution of the melt fraction for: $Pr = 41.04$ $Ra = 5\ 10^6$, $Ste = 0.04$

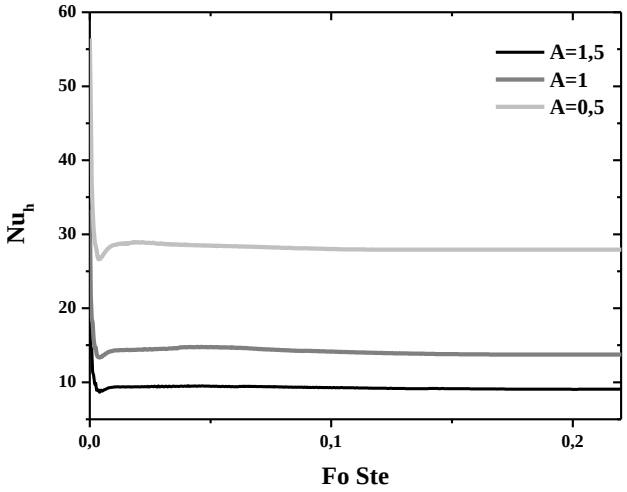

Fig. 27. Effects of the aspect ratio on the temporal variations of the average Nusselt number along the hot vertical wall for: $Pr = 41.04$, $Ra = 5\ \ 10^6$, $Ste = 0.04$

5.3 Comparison of the performance of three PCMs during the melting process in a rectangular enclosure

5.3.1 Purpose

The aim of this part is to compare the performance of the PCMs RT27, RT21 and RT35HC during the melting process in a rectangular enclosure. The PCMs are initially at their melting temperatures. The same geometric properties of the enclosure $(L = H = 0.05\ m)$ and the same temperature difference applied between the hot and the cold walls $(\Delta T = 4K)$ are used. For each study, the temperature of the cold wall is equal to the melting temperature of the PCM.

5.3.2 Performance analysis method

Preprints (www.preprints.org) | NOT PEER-REVIEWED | Posted: 4 March 2019 doi:10.20944/preprints201903.0034.v1

Two parameters are used to characterize the system performance, which are the melting fraction γ and the total energy stored in the PCM $Q_{tot}(Fo)$:

- The melting fraction $\gamma = \frac{V_{molten}}{V_{PCM}}$: it is defined in equation (15). Its time evolution characterizes the kinetic of the melting process.
- The total energy stored in the PCM during the dimensionless time interval $[0, Fo]$ $Q_{tot}(Fo)$:

  It reflects the capacity of the PCM to store thermal energy. During its melting, the PCM stores heat in form of sensible and latent heats. Thus, the total stored energy is given by:

$$Q_{tot}(Fo) = Q_{latent}(Fo) + Q_{sensible}(Fo), \quad (16)$$

$Q_{latent}(Fo)$ represents the stored latent heat. It is expressed as:

$$Q_{latent}(Fo) = \gamma \ \Delta H_{s\text{-}l}, \quad (17)$$

$Q_{sensible}(Fo)$ refers to the stored sensible energy. Since the PCMs used in the three studies are initially at their melting temperature, the storage of sensible energy took place only in the liquid PCM. This form of energy is defined as:

$$Q_{sensible}(Fo) = \sum_{cells} Q_{sensible,ij}(Fo), \quad (18)$$

where $Q_{sensible,ij}(Fo)$ represents the energy stored in a sensible form in a control volume V_{ij} around a node (i, j). It is expressed as follow:

$$Q_{sensible,ij}(Fo) = C_p(T_{ij} - T_m) \ \mathbf{if} \ f_{lij} = 1 \ , \quad (19)$$

T_m refers to the melting temperature of a paraffin.
Based on the dimensionless temperature, this form of energy is defined as

$$Q_{sensible,ij}(Fo) = C_p \ \Delta T \ \theta_{ij} \ \mathbf{if} \ f_{lij} = 1 \ , \quad (20)$$

$$Q_{sensible,ij}(Fo) = 0 \ \mathbf{if} \ f_{lij} < 1 \ , \quad (21)$$

A subroutine is added to the Fortran program of Fteiti et *al*. in order to calculate these forms of energy during the melting process.

5.3.3 Comparison of the performance of RT27, RT21 and RT35HC

The resulting dimensionless parameters which govern the melting process of each type of paraffin in a rectangular enclosure are summarized in **Table 7.**

Preprints (www.preprints.org) | NOT PEER-REVIEWED | Posted: 4 March 2019 doi:10.20944/preprints201903.0034.v1

Table 7 . Dimensionless parameters used in the studies

Paraffin	Ra	Pr	Ste	A
RT27	$5\ 10^6$	41.04	0.04	1
RT21	$1.8\ 10^7$	98	0.108	1
RT35HC	$8.3\ 10^6$	27	0.033	1

The comparison of the performance of the three types of paraffin is carried out in this part. It should be noted that the dimensionless time Fo will be converted to the time in hours during the illustration of the comparison's results in the followings paragraphs by using this expression: $t(\text{hours}) = \frac{1}{3600} Fo \frac{H^2}{\alpha}$. This is explained by the fact that since the PCMs doesn't have the same thermophysical properties, a fixed Fo doesn't correspond to the same time in hours for the three PCMs. That's why the use of Fo will hamper the comparison of their performance.

- **Comparison based on the kinetic criteria of the melting process**

The time evolutions of the melt fraction of RT27, RT21, RT35HC are displayed in **Fig. 28**. It can be observed from this figure that the more rapid melting phenomenon is attributed to RT21 followed by RT35HC and RT27. For a deep comparison between the three PCMs, the paraffin RT27 is taken as a reference. **Table. 8.** summarizes the melting time ratio for the three PCMs where this parameter is defined as the melting time of a PCM to the melting time of RT27. In fact, it was showed that the time required for the melting of RT21 and RT35HC are 28% and 12% less than that of RT27, respectively. Consequently, among the three PCMs used in this study, RT21 is the more performant from the kinetically viewpoint of the melting process. It is followed by RT35HC and RT27.

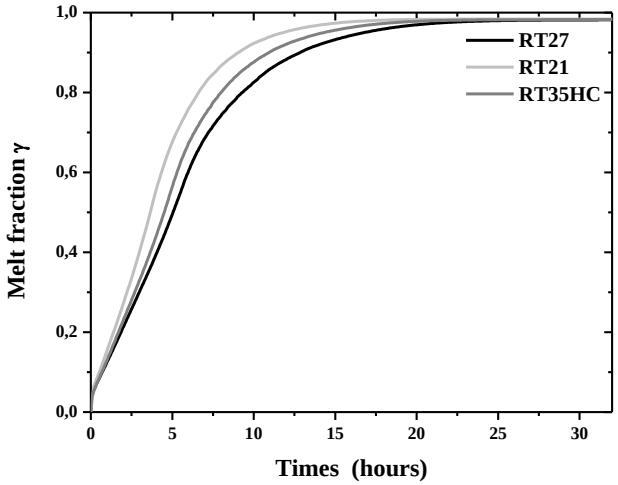

Fig. 28. Time evolution of the melt fraction for different PCMs

Preprints (www.preprints.org) | NOT PEER-REVIEWED | Posted: 4 March 2019 doi:10.20944/preprints201903.0034.v1

Table 8. Melting time ratios for different PCMs

PCM	Melting time ratio
RT27	1
RT21	0.72
RT35HC	0.88

- **Comparison based on the total PCM energy storage**

Fig. 29., Fig. 30 and Fig. 31 illustrate the temporal increase of the sensible, latent and total energies stored in RT27, RT21 and RT35HC respectively. Careful inspection for the results obtained for each PCM discloses that at a first stage of the melting process, the evolution of the latent and the total stored energies versus time are confused . This indicates that at this stage the energy is stored only in a latent form since the PCM is initially at its melting temperature. As the melting process evolves, the PCM stores energy in both forms latent and sensible heats. But, the majority of energy is stored in a latent form. In fact, the analysis of the results of **figures 29, 30 and 31** reveals that Q_{latent} represents 98%, 95% and 98.5% from the total stored energy in RT27, RT21, RT35HC, respectively during 32 hours.

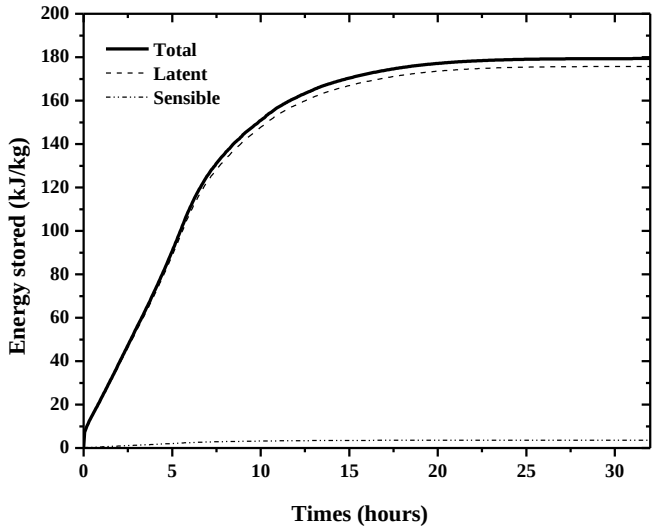

Fig. 29. Sensible, latent and total energies stored in RT27

Preprints (www.preprints.org) | NOT PEER-REVIEWED | Posted: 4 March 2019 doi:10.20944/preprints201903.0034.v1

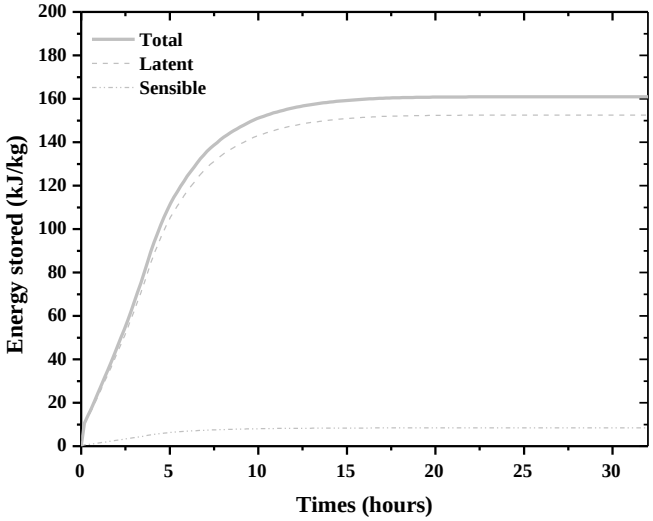

Fig. 30. Sensible, latent and total energies stored in RT21

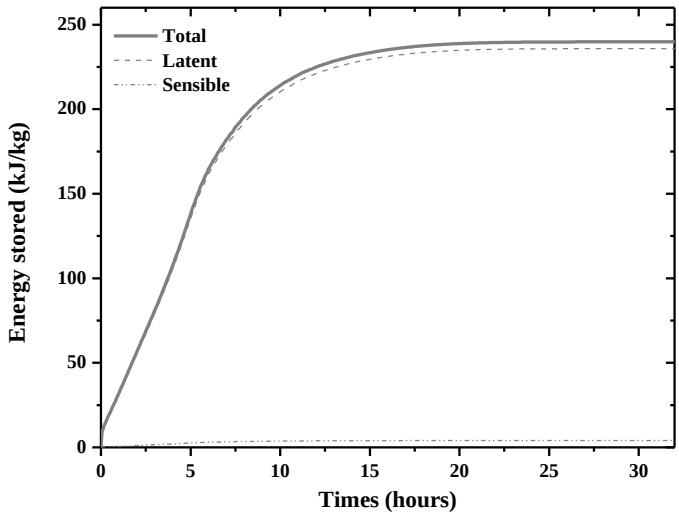

Fig. 31. Sensible, latent and total energies stored in RT35HC

Fig. 32. displays the time evolution of the total energy stored in RT27, RT21 and RT35HC. Deep examination of this figure inferred that RT35HC has the highest energy storage capacity which is 33% and 49% greater than RT27 and RT21, respectively during 32 hours. The comparison between RT27 and RT21 shows that the amount of energy stored in RT21 is higher than that stored in RT27 for $t < 10$ hours. At $t = 10$ hours, RT27 and RT21 have the same heat storage's capacity. Then, the performance of RT21 is reduced since it stores less energy than RT27.

Preprints (www.preprints.org) | NOT PEER-REVIEWED | Posted: 4 March 2019 doi:10.20944/preprints201903.0034.v1

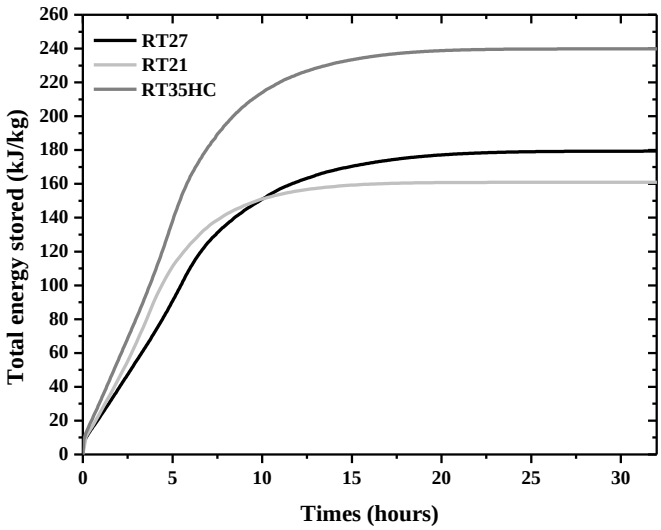

Fig. 32. Time evolution of the total energy stored in different PCMs: RT27, RT21, RT35HC

Since the majority of the energy stored in each PCM is in a latent form as it was clarified in the previous paragraph, the explanation of the findings of **Fig. 32** is carried out through the analysis of the time evolution of this form of energy for the three PCMs (**Fig. 33)** and the reference to the time evolution of the melting fraction of them (**Fig. 28).** In this context, it is important to mention that at a fixed time, the amount of the energy stored in a latent form in a PCM depends on the melt fraction obtained at this time and the latent heat of fusion $\Delta H_{s\text{-}l}$ of the PCM. Hence, it is a contribution of a parameter related to the kinetic of the melting process and thermophysical property of the PCM.

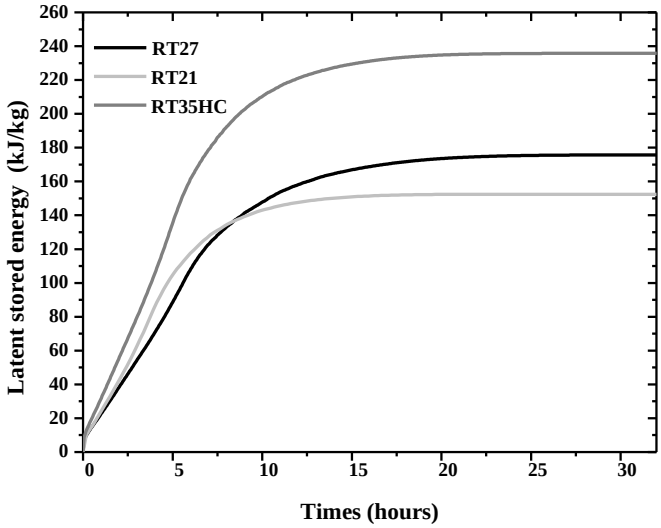

Fig. 33. Time evolution of the latent stored energy in different PCMs: RT27, RT21, RT35HC

Based on these concepts, deep examination of **Fig. 28** and **Fig. 33**. leads to the followings explanations. It is obvious that RT35HC stores more energy in a latent form than RT27 at different times since it

Preprints (www.preprints.org) | NOT PEER-REVIEWED | Posted: 4 March 2019 doi:10.20944/preprints201903.0034.v1

has larger melting fraction at each time and higher latent heat of fusion ΔH_{s-l} than that of RT27.

The comparison between the results found for RT35HC and RT21 reveals that despite that RT35HC melts more slowly than RT21, its capacity to store energy in a latent form is higher than RT21. This result can be explained by the discrepancy between the latent heats of fusion of the two PCMs. In fact, ΔH_{s-l} of RT35HC is 67% larger than that of RT21. Thus , at a fixed time, RT35HC has a less liquid fraction than RT21 but its large latent heat allows it to absorb more energy than RT21 .

As a conclusion , the comparison of the results of the latent heat stored in RT35HC to those in RT27 and in RT21 justifies the results found for the comparison between the total heat stored in RT35 HC to the other PCMs.

Concerning the comparison between RT27 and RT21, the results of **Fig. 28** and **Fig.29** found for t <8.4 hours can be explained as follow: on the one hand, during this period, RT21 melts more rapidly than RT27. In fact, it can be noticed from **Fig.28** that at t=8.2 hours, the melt fractions of RT21 and RT27 reaches 87% and 75%, respectively. On the other hand, for t < 8.4 hours, it should be noted from **Fig. 33** that despite that the latent heat of RT21 is 14.4% less than RT27, it stores more energy in a latent form than RT27. The coupling of these two ideas permits to conclude that during this period, the effect of the increase of the melt fraction of RT21 compared to that of RT27 on the amount of energy stored in a latent form exceeds the effect of the weakness of the latent heat ΔH_{s-l} of RT21 compared to that of RT27. This leads to a higher energy stored in RT21 in latent form than that in RT27.

For t= 8.4 hours, RT21 and RT27 stores the same amount of energy in a latent form. This is explained by the fact that at this instant $(\gamma\, \Delta H_{s-l})_{RT21} = (\gamma\, \Delta H_{s-l})_{RT27}$

For t > 8.4 hours, RT21 stores less energy in a latent form than that of RT27. This result is explained as follow: **Fig. 28** shows that the speed of the melting process of RT21 and RT27 decreases for t > 8.4 hours which implies a decrease in the melting rate of the two PCMs during this period compared to that for t < 8.4 hours. Consequently, the effect of the melt fraction on the latent energies stored in these PCMs decreases compared to that for t < 8.4 hours Thus, the amount of energy stored in a latent form becomes governed by the latent heat of fusion ΔH_{s-l} of the PCM. Therefore, since RT21 has a less ΔH_{s-l} than RT27, its capacity to store energy in a latent form is less that of RT27 for t > 8.4 hours. Hence, the difference between the latent energies stored in RT27 and RT21 found for t > 8.4 hours is due to discrepancy between their latent heats of fusion.

As a conclusion, the coupling of the results found for the time evolution of the total and the latent energies stored in RT27 and RT21 permit to affirm the following conclusions:

For **0 < t < 8.4 hours** , the total energy stored in RT21 is higher than that in RT27 because RT21 stores more energy in a latent form than RT27.

For **t =8.4 hours** , the total energy stored in RT21 is 3.3% greater than that in RT27 despite that the two PCMs stores the same amount of energy in a latent form. This results is due to the discrepancy between the sensible stored energies in them. In fact, at this instant, RT21 stores 7.75 kJ/kg while RT27 stores 3 kJ/kg. More details about the time evolutions of this form of energy in these PCMs are depicted in **Fig. 34.**

Preprints (www.preprints.org) | NOT PEER-REVIEWED | Posted: 4 March 2019 doi:10.20944/preprints201903.0034.v1

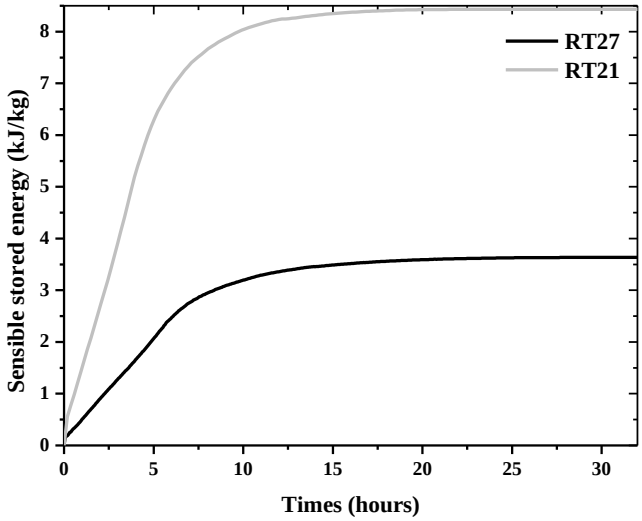

Fig. 34. Time evolution of the sensible stored energy in RT27 and RT21

For 8.4 < t < 10 hours, on the one side, the total heat storage capacity of RT21 is slightly more than that of RT27. On the other side, RT21 stores little less energy in a latent form than RT27. Hence, the result found concerning the total stored energy is attributed to the fact that heat stored in a sensible form in RT21 is greater than that in RT27 **(Fig. 34).** The analyze of the results found for 8.4 < t < 10 hours discloses that the effect of the discrepancy in the sensible stored energies in RT27 and RT21 on the total stored energy is observed only when the difference between the latent stored energy is slight .

For t= 10 hours **,** the two PCMs stores the same total energy.

For t > 10 hours, the amount of the total energy stored in RT21 is less than that in RT27 since the RT21 stores less energy in a latent form than RT27 with a large difference between this form of energy in the two PCMs compared to the previous time interval.

5. Conclusion

This paper reports an experimental thermophysical characterization of three types of paraffin waxes (RT27, RT21 and RT35HC) and a numerical study of their melting in a rectangular enclosure heated isothermally at its left vertical side. The first part of the numerical investigation was dedicated to the study of the thermal behavior of RT27 during its melting process. Solid-liquid interface shape, temperature field and average Nusselt number along the hot vertical wall were used to understand the heat transfer mechanisms during this phenomenon. Results showed that the conduction is the dominant heat transfer mode in the beginning of the melting which is followed by a transition regime characterized by the coexistence of the conduction and the natural convection. Then, the natural convection becomes the dominant heat transfer mode. The intensity of the convection currents decreases slightly as the solid-liquid interface reaches the opposite vertical wall. The effects of the Rayleigh number and the aspect ratio of the enclosure on the melting process of RT27 were also studied in this part. It was revealed that the intensity of the natural convection increases as the Rayleigh number is higher and the aspect ratio is smaller. This intensification induces an acceleration

of the melting phenomenon. In the second part of the numerical study, a comparison of the performance of the paraffin RT27, RT21 and RT35HC during their melting process in a rectangular enclosure was carried out. The same geometric properties of the enclosure and the same temperature difference applied between the hot and the cold walls are used for the three PCMs. The comparison was conducted based on two criteria**: (1)** a kinetic criteria which is the time evolution of the melt fraction and **(2**) the heat storage capacity of the PCMs. Results showed that from a kinetically viewpoint, RT21 is the most performant which is followed by RT35HC and RT27.In fact, it was revealed that the time required for the melting of RT21 and RT35HC are 28% and 12% less than that of RT27, respectively. In term of the heat storage capacity, it was shown that RT35HC is the most efficient since that it stores the highest total energy compared to the other PCMs which is 33% greater than RT27 and 49% more than that of RT21 during 32 hours. As a conclusion, for the same configuration, the choice of the appropriate PCM among the three paraffins used in this study depends on the criteria fixed for the choice.

References

1. B. Zalba, J.M. Marìn, Cabeza. L.F, H. Mehling, Review on thermal energy storage with phase change: materials, heat transfer analysis and applications, *Appl. Therm. Eng*. 23 (2003) 251–283.

2. A. Sharma, V.V. Tyagi, C.R. Chen, D. Buddhi, Review on thermal energy storage with phase change materials and applications, *Renew. Sustain. Energy Rev*. 13 (2009) 318–345.

3. Y. Jellouli, R. Chouikh, A. Guizani, A. Belghith, Numerical study of the moving boundary problem during melting process in a rectangular cavity heated from below, *Am. J. Appl Sci* 4 (2007) 251–256.

4. H. Shokouhmand, B. Kamkari, Experimental investigation on melting heat transfer characteristics of lauric acid in a rectangular thermal storage unit, *Exp. Therm. Fluid Sci* 50 (2013) 201–212.

5. CJ. Ho, KC. Liu, WM. Yan, Melting processes of phase change materials in an enclosure with a free-moving ceiling: An experimental and numerical study, *Int. J. Heat Mass Transfer* 83 (2015) 222–228.

6. Y. Zhang, Z. Chen, Q. Wang, Q. Wu, Melting in an enclosure with discrete heating at a constant rate, Exp. *Therm. Fluid Therm Sci* 6 (1993) 196–201.

7 Z. Jianhua, C. Zhongqi, L. Dengying, L. Ji, Experimental study on melting in a rectangular enclosure heated below with discrete heat sources, *Int. J. Therm Sci* 10 (2001) 254–259.

8. X. Sun, Q. Zhang, MA. Medina, KOk. Lee, Experimental observations on the heat transfer enhancement caused by natural convection during melting of solid–liquid phase change materials (PCMs), *Appl. Energy* 162 (2016) 1453-1461.

9. M. Aadmi, M. Karkri, M. El Hammouti, Heat transfer characteristics of thermal energy storage of a composite phase change materials: Numerical and experimental investigations, Energy 92 (2014) 372:381.

10. AR. Archibold, MM. Rahman, D. Yogi Goswami, EK. Stefanakos, Analysis of heat transfer and fluid flow during melting inside a spherical container for thermal energy storage, *Applied Thermal Engineering* 64 (2014) 396-407.

11. M. Aadmi, M. Karkri, M. El Hammouti, Heat transfer characteristics of thermal energy storage for PCM (phase change material) melting in horizontal tube: Numerical and experimental investigations, *Energy* 85 (2015) 339-352.

12. RUBITHERM GmbH - www.rubitherm.com.

13. M. Lachheb, M. Karkri, Sassi Ben Nasrallah, Development and thermal characterization of an innovative

gypsum-based composite incorporating phase change material as building energy storage system, *Energ Buildings* 107 (2015) 93 -102

14. Y. He, Rapid thermal conductivity measurement with a hot disk sensor Part 1Theoretical considerations, *Thermochim Acta*, 436 (2005), 122-129

15. AD. Brent, VR. Voller, KJ .Reid, Enthalpy-porosity technique for modeling convection–diffusion phase change: application to the melting of pure metal, *Numer. Heat Transfer* 13 (1988) 297–318.

16. VR. Voller, C. Prakash, A fixed grid numerical modeling methodology for convection-diffusion mushy region phase-change problems, *Int. J. Heat Mass Transfer* 30 (1987) 1709–1719.

17. M. Fteiti, S. Ben Nasrallah, Numerical analysis of a latent heat thermal energy storage system, *Int. J. Heat Technology* 1 (2004) 161-164

18. BR. Baliga, Patankar, A new finite-element formulation for solving convection-diffusion problems, *Numer. Heat Transfer* 3(1980) 393–409.

19. BR. Baliga, SV. Patankar, A Control Volume Finite Element method for two dimensional fluid flow and heat transfer, Numer. Heat Transfer 6 (1983) 245–282.

20. M. Fteiti, S .Ben Nasrallah, Numerical study of interaction between the fluid structure and the moving interface during the melting from below in a rectangular closed enclosure, *Comput Mech 35 (2005) 161 – 169.*

21. AJL. Jesus, SCC. Nunes, MR. Silva , AM. Beja, JS. Redinha, Erythritol: crystal growth from the melt. *Int J Pharm* 388(2010)129–35.

22. EB. Sirota, DM. Singer, Phase transitions among the rotator phases of the normal alkanes. J Chem Phys 101 (1993) 10873–82.

23. J. Doucet, I. Denicolo, A. Craievich, A .Collet, Evidence of a phase transition in the rotator phase of the odd-numbered paraffins C H and C H. *J Chem Phys* 75 (1981) 5125 -7

24. S. Sari-Bey, M.Fois, I. Krupa, L. Ibos, B. Benyoucef, Y. Candau, Thermal characterization of polymer matrix composites containing microencapsulated paraffin in solid or liquid state, Energy Convers Manag 78 (2014) 796–804

25. P. Jany, A. Bejan, Scaling theory of melting with natural convection in an enclosure, *Int. J. Heat Mass Transfer* 31 (1988) 1221–1235.